LEAD ARTICLE

Acta Cryst. (1994). A**50**, 261–286

Convergent-Beam Electron Diffraction

BY MICHIYOSHI TANAKA

Research Institute for Scientific Meaurements, Tohoku University, Sendai 980, *Japan*

(*Received* 2 *June* 1993; *accepted* 28 *September* 1993)

Abstract

Symmetry determination of three-dimensional (usual) crystals, four-dimensional (one-dimensionally incommensurate) crystals and five- and six-dimensional crystals (quasicrystals) by convergent-beam electron diffraction is described and demonstrated using real materials. Crystal structure refinement based on the dynamical theory of electron diffraction is described for the low-temperture phase of $SrTiO_3$.

1. Introduction

Recent crystallographic studies by convergent-beam electron diffraction (CBED) originated with Goodman & Lehmpfuhl (1965), although earlier work by Kossel & Möllenstedt (1939) was done about five decades ago. They obtained CBED patterns by converging a conical electron beam of an angle of more than 10^{-3} rad on a small area of a specimen (~300 Å ∅), which had a uniform thickness and no bending. Instead of the usual diffraction spots, diffraction disks are produced. The diffracted intensity in a disk can be compared with that calculated on the basis of the dynamical theory of electron diffraction. The method corresponding to CBED in the field of light optics is the conoscope method. Using a conoscope, we can identify a crystal as isotropic, uniaxial or biaxial and determine the optic axis and the signs of birefringence. When CBED, a conoscope method using an electron beam, is utilized, more basic properties of a crystal – the crystal point groups and space groups – can be determined.

Point- and space-group determinations have previously been carried out by X-ray diffraction. This method, to which the kinematical diffraction theory is applicable, cannot determine whether a crystal is polar or non-polar unless anomalous dispersion is utilized. As a result, the X-ray diffraction method can only identify 11 Laue groups among 32 point groups. CBED, based fully upon dynamical diffraction, can distinguish polar crystals from nonpolar crystals, thus allowing the unique identification of all the point groups by inspection of the symmetries appearing in CBED disks. For the theory of point-group determination, see Goodman (1975), Tinnappel (1975), Buxton, Eades, Steeds & Rackham (1976), Tanaka, Saito & Sekii (1983) and Eades (1988*a*).

Furthermore, CBED enables us to identify the presence of 2_1 screw axes and glide planes through a conspicuous dynamical diffraction effect. When a crystal has these axes or planes, special extinction lines appear in kinematically forbidden reflections, the lines being called dynamical extinction lines or Gjønnes–Moodie (*G–M*) lines. By examination of whether *G–M* lines are formed or not in kinematically forbidden reflections, most space groups can be identified (Gjønnes & Moodie, 1965; Tanaka, Sekii & Nagasawa, 1983; Eades, 1988*b*). Therefore, CBED is much superior to the X-ray method in determining crystal point groups and space groups.

The repetition of a unit cell, the translational symmetry, is a characteristic feature of crystals. An exception – incommensurate structure – appears in a crystal over a certain temperature range. The period of this structure does not coincide rationally with that of the protophase. The structure, however, recovers lattice periodicity in a space higher than three dimensions. The one-dimensionally incommensurate structure is described by a three-dimensional section of a crystal in four-dimensional space. The first study of an incommensurate structure was performed by Steeds *et al.* (1985) on $NiGe_{1-x}P_x$. Two examples of studies were carried out on $Sr_2Nb_2O_7$ and Mo_8O_{23} by Tanaka, Terauchi & Kaneyama (1988); however, four-dimensional analysis of the CBED patterns obtained from incommensurately modulated crystals was not carried out in those

Dr M. Tanaka has been a leading exponent of the convergent-beam electron diffraction technique for many years. Working closely with the JEOL company in instrumentation development, his group in the Physics Department at Tohoku have consistently produced many of the highest-quality data and pioneered many innovative techniques. His two volumes of collected CBED patterns (with M. Terauchi and T. Kaneyama) have become the standard reference work for all researchers and students in the field.

studies. Recently, the point- and space-group-determination method for these crystals has been established by Terauchi & Tanaka (1993) and Terauchi, Takahashi & Tanaka (1994).

The discovery of an aluminium–manganese alloy (Shechtman, Blech, Gratias & Cahn, 1984) that gives sharp diffraction spots with an icosahedral symmetry has had a great impact on crystallography and solid-state physics. It has revealed the existence of a new structural order (quasicrystal). The quasicrystal is defined to have quasiperiodic long-range structural order with a noncrystallographic point group and to have a self-similarity transformation. The discovery of quasicrystals has accelerated the theoretical development of crystallography in high-dimensional spaces. Icosahedral quasicrystals are regarded as six-dimensional crystals; decagonal ones as five-dimensional crystals. CBED is definitely the best method to investigate the symmetry of this new class of structural order (Tanaka, Terauchi, Hiraga & Hirabayashi, 1985; Bendersky & Kaufman, 1986; Tanaka, Terauchi, Hiraga & Hirabayashi, 1987).

CBED is now entering a stage of quantitative studies. Crystal structure analysis or the determination of atom positions using CBED patterns was carried out first for AuGeAs by Vincent, Bird & Steeds (1984) and later for metastable Al–Ge by Vincent & Exelby (1990). They applied a quasi-kinematical theory to the fitting between experimental and calculated intensities. The first determination of atom positions using the dynamical theory was performed by Tanaka & Tsuda (1990, 1991) for the low-temperature phase of $SrTiO_3$. This work proved that the CBED method enables structure refinement based on the dynamical diffraction theory. Bird & Saunders (1992*a*,*b*) intended to develop an *ab initio* structure-determination method using the dynamical diffraction theory. They stated that the method is feasible on the basis of a test on GaP. Recent publications concerning crystal structure analysis are referred to in their papers.

In the present paper, we first describe the symmetry determination of three-dimensional (usual) crystals, then that of four-dimensional (incommensurate) crystals and of five- and six-dimensional crystals (quasicrystals), and finally crystal structure refinement. We omit the other important application of CBED, the identification of lattice defects. Readers who have an interest in this topic may refer to a review paper by Tanaka, Terauchi & Kaneyama (1991). In addition, we must refer to a chapter of a book on CBED by Eades (1992), which explains experimental techniques, symmetry determinations *etc.*, and to a timely book on CBED written by Spence & Zuo (1992), which deals with all matters concerning the CBED method and its applications to date.

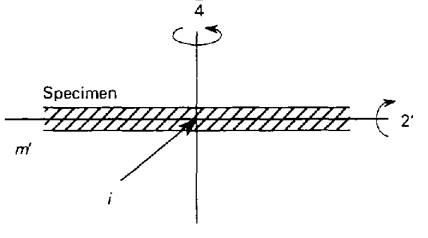

Fig. 1. Four symmetry elements m', i, $2'$ and $\bar{4}$ of an infinitely extended parallel-sided specimen.

Table 1. *Two- and three-dimensional symmetry elements of an infinitely extended parallel-sided specimen*

Symbols in parentheses show CBED symmetries appearing in dark-field disks.

Two-dimensional symmetry elements	Three-dimensional symmetry elements
1	m' (1_R)
2	i (2_R)
3	$2'$ (m_2, m_R)
4	$\bar{4}$ (4_R)
6	
m	

2. Symmetry determination of three-dimensional crystals

2.1. *Point-group determination*

2.1.1. *Symmetry elements of a specimen and diffraction groups.* The point-group-determination method given by Buxton *et al.* (1976) is described with the aid of the description by Tanaka, Saito & Sekii (1983). They considered a perfect crystalline specimen that is parallel sided and infinite in two dimensions. The symmetry elements of the specimen form 'diffraction groups', which are isomorphic to the point groups of diperiodic plane figures and Shubnikov groups of colored plane figures. The diffraction groups of a specimen are determined from the symmetries of CBED patterns taken at various orientations of the specimen. The crystal point group of the specimen is identified by referring to a table that gives the relation between diffraction groups and crystal point groups.

A specimen that is parallel sided and is infinitely extended in the x and y directions has ten symmetry elements. The symmetry elements consist of six two-dimensional symmetry elements and four three-dimensional ones. The operation of the former elements transforms an arbitrary coordinate (x, y, z) into (x', y', z), z remaining the same. The operation of the latter transforms a coordinate (x, y, z) into (x', y', z'), where $z' \neq z$. A vertical mirror plane m and

Table 2. *Symmetry elements of an infinitely extended parallel-sided specimen and diffraction groups*

	1	2	3	4	6	m	$2m(m)$	$3m$	$4m(m)$	$6m(m)$	
1	1	2	3	4	6	m	$2m(m)$	$3m$	$4m(m)$	$6m(m)$	10
$(m')1_R$	1_R	21_R	31_R	41_R	61_R	$m1_R$	$2m(m)1_R$	$3m1_R$	$4m(m)1_R$	$6m(m)1_R$	10
$(i)2_R$	2_R	(21_R)	6_R	(41_R)	(61_R)	$2_Rm(m_R)$	$[2m(m)1_R]$	$6_Rm(m_R)$	$[4m(m)1_R]$	$[6m(m)1_R]$	4
$(2')m_R$	m_R	$2m_R(m_R)$	$3m_R$	$4m_R(m_R)$	$6m_R(m_R)$	$[2_Rm(m_R)]$ $(m1_R)$	$[2m(m)1_R)]$ $[4_R(m)m_R]$	$(3m1_R)$ $[6_Rm(m_R)]$	$[4m(m)1_R]$	$[6_Rm(m_R)]$	5
$(\bar{4})\ 4_R$		4_R		(41_R)		$4_Rm(m_R)$	$[4_Rm(m_R)]$		$[4m(m)1_R]$		2

$1_R \cdot 2_R = 2$, $2_R \cdot 2_R = 1$, $m_R \cdot 2_R = m$, $4_R \cdot 2_R = 4$, $1_R \cdot m_R = m \cdot m_R$, $1_R \cdot 4_R = 4 \cdot 1_R$, $m_R \cdot 4_R = m \cdot 4_R$.

one-, two-, three-, four- and sixfold rotation axes that are parallel to the surface normal **z** are the two-dimensional symmetry elements. The three-dimensional symmetry elements consist of a horizontal mirror plane m', an inversion center i, a horizontal twofold rotation axis $2'$ and a fourfold rotary inversion $\bar{4}$ whose axis is parallel to the surface normal as shown in Fig. 1. Table 1 lists these symmetry elements. Symbols in parentheses express symmetries of CBED patterns expected from three-dimensional symmetry elements.

The diffraction groups are constructed by combining these symmetry elements (Table 2). Two-dimensional symmetry elements and their combinations are given in the first row of the table. The third symmetry m in parentheses is introduced automatically when the first two symmetry elements are combined. Three-dimensional symmetry elements are given in the first column. The equations given below the table show that any additional three-dimensional symmetries do not appear by the combination of two symmetry elements in the first column. As a result, 31 diffraction groups are produced by combination of the elements in the first column with those in the first row. Diffraction groups in parentheses have already appeared somewhere. In row 5, two diffraction groups appear in three columns. These two groups are produced when the symmetry elements are combined at relatively different orientations. In row 6, five places are empty because a fourfold rotary inversion cannot be combined with threefold and sixfold axes. In the last column, the number of independent diffraction groups is given in each row, the sum of the numbers being 31.

2.1.2. *Identification of three-dimensional symmetry elements.* It is difficult to visualize symmetries of CBED patterns expected from the three-dimensional symmetry elements. The reason is that, if we consider the direct operation of a three-dimensional symmetry element, a specimen has to be set upside down, which is not realistic in usual experiments. The reciprocity theorem of scattering theory enables us to clarify the symmetries of CBED patterns expected from the three-dimensional symmetry elements (Pogany & Turner, 1968). The theorem is stated, referring to Fig. 2, as follows: the amplitude of a wave at B that originates from a source at A and is scattered by P is equal to the scattered amplitude at A originating from the same source placed at B. We consider, as an example, the symmetry of a CBED pattern expected from an inversion center.

Fig. 3 shows stereographic projections, where the surface normal is taken to be parallel to the zone axis as shown by the cross (+). The incoming beam I running downwards is represented by the filled circle in Fig. 3(a). The outgoing beam O is represented by an empty circle. An outgoing diffracted beam G is also represented by an empty circle, which is produced by displacing the outgoing beam O by the reflection vector G. Then, the incoming beam and the diffracted beam are symmetric about the point $G/2$. When the stereo projection of the incoming beam comes to the point $G/2$, the diffracted beam is set exactly to the Bragg condition. To simplify the diagrams, only the incoming beam I and the diffracted beam G are shown in Fig. 3(b). In Fig. 3(c), the beam running reciprocal to Fig. 3(b) is shown, where the incoming beam (filled circle) and the diffracted beam (empty circle) run upward. The reciprocity theorem tells us that the intensities of the diffracted beams in Figs. 3(b) and (c) are the same. The operation of an inversion center on the beams in Fig. 3(c) produces an incoming beam and a diffracted beam $-G$ that run downward and are symmetric about the point $-G/2$ (Fig. 3d). This downward-going diffracted beam $-G$ and the diffracted beam G in Fig. 3(a) are shown in Fig. 3(e). The two disks, each of which contains one of the beams, represent CBED disks, the shape and size of which are usually determined

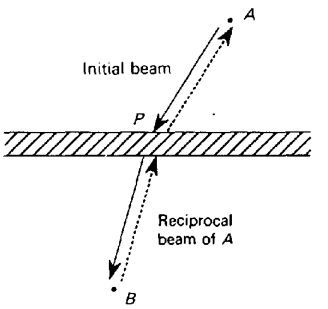

Fig. 2. Diagram to illustrate reciprocity. The solid line shows the beam initially considered. The dotted line shows a beam running opposite to the initial beam.

by the condenser aperture. The symmetry between the patterns of the two disks in Fig. 3(*e*) is called 2_R. The symbol is related to the operations that translate the diffracted beam in one disk into that in the other disk; that is, the operation of a twofold rotation about the zone axis (symbol 2) on the beam in the G reflection yields the cross (+) in the $-G$ reflection. A rotation of the cross by an angle π (subsymbol R) about the point $-G/2$ produces the diffracted beam $-G$ designated by the empty circle. The combination of the two operations is written as 2_R. The symmetry is sometimes called translational symmetry because the pattern of the $+G$ disk coincides with that of the $-G$ disk by a translation. The pattern of a dark-field disk in which an exact Bragg position is set at the disk center is called a dark-field (DF) pattern. Symmetries of CBED patterns expected from other three-dimensional symmetry elements were clarified with the help of the reciprocity theorem (Goodman, 1975; Buxton *et al.*, 1976). The CBED symmetries obtained are illustrated in Fig. 4. A horizontal twofold axis 2′, a horizontal mirror plane m' and a fourfold rotary inversion $\bar{4}$ produce symmetries m_R (m_2), 1_R and 4_R, respectively. The operation m_R is shown, in Fig. 4(*a*), to be equivalent to the sequential operation of the mirror m, transforming the open-circle (○) beam of the G reflection into the + beam of the G' reflection, and the operation R (rotation of the disk by π about the point $G'/2$), which then transfers this beam to the ○ position of the G' reflection. The combination of the two operations is written as m_R. When the twofold axis is parallel to the diffraction vector G, a mirror line, perpendicular to the vector G and passing through the point $G/2$, appears in the CBED disk. The mirror symmetry is called m_2, the suffix 2 being given to distinguish the symmetry from the mirror symmetry originating from a vertical mirror plane. The operation 1_R (Fig. 4*b*) for a horizontal mirror plane is a combination of a rotation of 2π about a zone axis (symbol 1) and a rotation of π about an exact Bragg position. The symmetry 4_R (Fig. 4*c*) can be understood in a similar manner.

The four three-dimensional symmetry elements were found to produce different symmetries in CBED patterns. These facts enable us to unambiguously identify these symmetry elements from the symmetries of CBED patterns.

2.1.3. *Identification of two-dimensional symmetry elements.* Because of dynamical diffraction effects, two-dimensional symmetry elements, which belong to a zone axis, exhibit their symmetries in CBED patterns taken at the electron incidence parallel to the zone axis. The patterns are called zone-axis patterns (ZAPs). A ZAP contains a bright-field (BF) pattern and a whole pattern. The BF pattern is the pattern appearing in the BF disk. The whole pattern is composed of the patterns of the BF disk and the diffracted disks. It should be noted that, since these diffracted disks do not contain exact Bragg positions, the patterns of the disks are not called dark-field (DF) patterns. The two-dimensional symmetry elements m, 1, 2, 3, 4 and 6 yield, respectively, a symmetry m_v and one-, two-, three-, four- and sixfold rotation symmetries in the whole pattern, where the suffix v of m_v is given to distinguish the symmetry from the mirror symmetry m_2 originating from a horizontal twofold axis. All the two-dimensional symmetry elements can be identified from whole-pattern symmetries.

2.1.4. *Point-group determination.* All the symmetry elements of an infinitely extended parallel-sided specimen or all the diffraction groups can be identified by the symmetries of whole and DF patterns. It

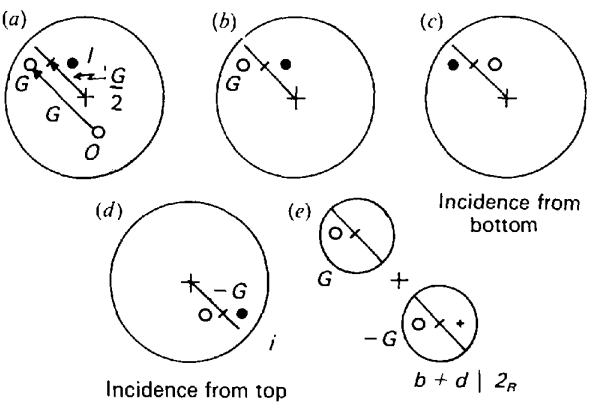

Fig. 3. Illustration of the stereographic method to obtain CBED symmetries from an inversion center (see text).

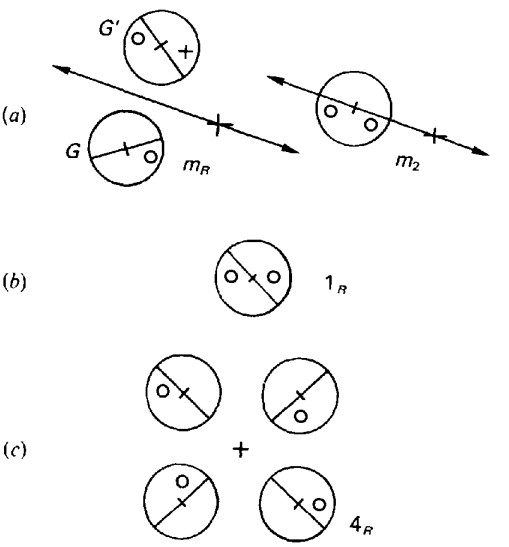

Fig. 4. Symmetries appearing in dark-field patterns. (*a*) m_R and m_2, (*b*) 1_R and (*c*) 4_R, originating from 2′, m' and $\bar{4}$, respectively.

Table 3. *Symmetries of zone-axis, dark-field and ±G CBED patterns*

(I) Diffraction group, (II) bright-field pattern, (III) whole pattern, (IV) dark-field pattern, (V) ±G patterns, (VI) projection diffraction group.

I	II	III	IV	V	VI
1	1	1	1	1	1_R
1_R	2 (1_R)	1	$2 = 1_R$	1	〃
2	2	2	1	2	21_R
2_R	1	1	1	2_R	〃
21_R	2	2	2	21_R	〃
m_R	m (m_2)	1	1 m_2	1 m_R 1	$m1_R$
m	m_v	m_v	1 m_v	1 m_v 1	〃
$m1_R$	$2mm$ $[m_v + m_2 + (1_R)]$	m_v	2 $2m_vm_2$	1 m_v1_R 1	〃
$2m_Rm_R$	$2mm_v$ $(2 + m_2)$	2	1 m_2	2 $2m_R(m_2)$	$2mm1_R$
$2mm$	$2m_vm_{v'}$	$2m_vm_{v'}$	1 m_v	2 $2m_{v'}(m_v)$	〃
2_Rmm_R	m_v	m_v	1 m_2 m_v	2_R $2_Rm_{v'}(m_2)$ $2_Rm_R(m_v)$	〃
$2mm1_R$	$2m_vm_{v'}$	$2m_vm_{v'}$	2 $2m_vm_2$	21_R $21_Rm_{v'}(m_v)$	〃
4	4	4	1	2	41_R
4_R	4	2	1	2	〃
41_R	4	4	2	21_R	〃
$4m_Rm_R$	$4mm$ $(4 + m_2)$	4	1 m_2	2 $2m_R(m_2)$	$4mm1_R$
$4mm$	$4m_vm_{v'}$	$4m_vm_{v'}$	1 m_v	2 $2m_{v'}(m_v)$	〃
4_Rmm_R	$4mm$ $(2m_vm_{v'} + m_2)$	$2m_vm_{v'}$	1 m_2 m_v	2 $2m_R(m_2)$ $2m_{v'}(m_v)$	〃
$4mm1_R$	$4m_vm_{v'}$	$4m_vm_{v'}$	2 $2m_vm_2$	21_R $21_Rm_{v'}(m_v)$	〃
3	3	3	1	1	31_R
31_R	6 $(3 + 1_R)$	3	2	1	〃
$3m_R$	$3m$ $(3 + m_2)$	3	1 m_2	1 m_R 1	$3m1_R$
$3m$	$3m_v$	$3m_v$	1 m_v	1 m_v 1	〃
$3m1_R$	$6mm$ $[3m_v + m_2 + (1_R)]$	$3m_v$	2 $2m_vm_2$	1 m_v1_R 1	〃
6	6	6	1	2	61_R
6_R	3	3	1	2_R	〃
61_R	6	6	2	21_R	〃
$6m_Rm_R$	$6mm$ $(6 + m_2)$	6	1 m_2	2 $2m_R(m_2)$	$6mm1_R$
$6mm$	$6m_vm_{v'}$	$6m_vm_{v'}$	1 m_v	2 $2m_{v'}(m_v)$	〃
6_Rmm_R	$3m_v$	$3m_v$	1 m_2 m_v	2_R $2_Rm_{v'}(m_2)$ $2_Rm_R(m_v)$	〃
$6mm1_R$	$6m_vm_{v'}$	$6m_vm_{v'}$	2 $2m_vm_2$	21_R $21_Rm_{v'}(m_v)$	〃

should be noted that a pair of DF patterns and four DF patterns are needed to identify symmetry elements i and $\bar{4}$, respectively, whereas one DF pattern is enough for m' and $2'$. A ZAP, or a combination of a whole pattern and the BF pattern included in the whole pattern, permits the identification of the symmetry element $\bar{4}$ because no other symmetry element exhibits fourfold symmetry in the BF pattern and twofold symmetry in the whole pattern. Some diffraction groups can also be determined by a ZAP without taking DF patterns. Therefore, a practical method to determine diffraction groups utilizes BF, whole, DF and ±G patterns.

The symmetries appearing in BF, whole, DF and ±G patterns are given for the 31 diffraction groups in Table 3 (Tanaka, Saito & Sekii, 1983), which is similar to Table 2 of Buxton *et al.* (1976). All the possible symmetries of DF and ±G patterns lying at various orientations are given in this table. When a BF pattern has a higher symmetry than the whole pattern, the symmetry elements that produce the former pattern are given in parentheses in column II except for the case of 4_R, where this effect arises because the sequential operation of 4 and R is indistinguishable from the single operation of 4, for the BF pattern. When two types of vertical mirror plane exist, these are distinguished by the symbols m_v and

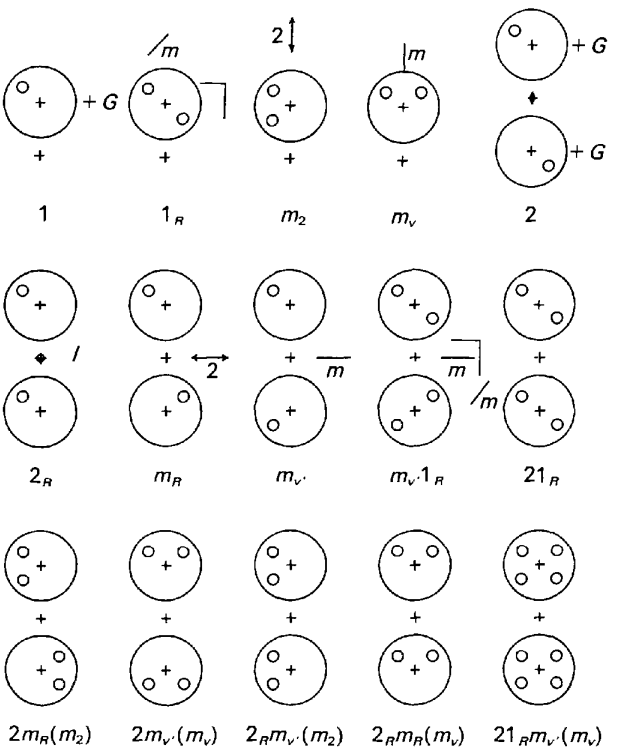

Fig. 5. Illustration of symmetries of dark-field patterns and ±G patterns.

Table 4. *Relation between diffraction groups and crystal point groups* [*courtesy of the Royal Society of London* (*Buxton, Eades, Steeds & Rackham*, 1976)]

	1	$\bar{1}$	2	m	2/m	222	mm2	mmm	4	$\bar{4}$	4/m	422	4mm	$\bar{4}$2m	4/mmm	3	$\bar{3}$	32	3m	$\bar{3}$m	6	$\bar{6}$	6/m	622	6mm	$\bar{6}$m2	6/mmm	23	m3	432	$\bar{4}$3m	m3m
$6mm1_R$																										X						
$3m1_R$																									X							
$6mm$																								X								
$6m_Rm_R$																							X									
61_R																						X										
31_R																					X											
6																				X												
6_Rmm_R																			X													X
$3m$																		X													X	
$3m_R$																	X													X		
6_R																X													X			
3															X												X					
$4mm1_R$														X																		X
4_Rmm_R													X																		X	
$4mm$												X																				
$4m_Rm_R$											X																			X		
41_R										X																						
4_R									X																							
4								X																								
$2mm1_R$							X							X												X		X				X
2_Rmm_R					X		X				X			X					X			X			X		X				X
$2mm$						X																			X							
$2m_Rm_R$						X						X		X										X			X		X			
$m1_R$						X							X	X										X	X					X		
m				X		X							X	X					X			X			X	X				X		
m_R			X			X	X		X	X		X	X	X				X			X			X	X	X		X		X	X	
21_R					X															X												
2_R		X			X			X			X				X		X			X			X				X		X			X
2			X															X														
1_R				X															X													
1	X		X	X		X	X		X	X		X	X	X		X		X	X		X	X		X	X	X		X		X	X	

$m_{v'}$. Plural symmetries seen in columns IV and V are obtained at exact Bragg settings of reflection disks appearing in different directions. Fig. 5 illustrates the symmetries of DF and $\pm G$ patterns given in Table 3. A diffraction group is determined from the four patterns, BF, whole, DF and $\pm G$, appearing in three photographs, although many groups can be determined from a set of BF and whole patterns or a set of BF, whole and DF patterns.

Possible point groups are selected from the diffraction group obtained by consulting Table 4 (Buxton *et al.*, 1976), in which the relation between the 31 diffraction groups and 32 crystal point groups is given. Each of 11 high-symmetry diffraction groups corresponds to one crystal point group. When plural point groups are obtained from a diffraction group, a different diffraction group has to be obtained at another zone axis and then point groups are selected. Then, a point group is identified by the selection of a common point group existing among the point groups obtained at the different zone axes.

High-symmetry zone axes have to be chosen for point-group determination because low-symmetry zone axes only exhibit a small number of crystal symmetries in CBED patterns. CBED is used to observe part of the symmetry of a given crystal; that is, CBED cannot be used to observe the crystal symmetries oblique to the incident beam and horizontal three-, four- and sixfold axes. Therefore, even for a crystal with a particular point group, different diffraction groups are expected at different crystal settings. Table 5 (Buxton *et al.*, 1976) shows all the

Table 5. *Diffraction groups expected at various crystal orientations for* 32 *point groups* [*courtesy of the Royal Society of London* (*Buxton, Eades, Steeds & Rackham*, 1976)]

Zone-axis symmetries							
Point group	⟨111⟩	⟨100⟩	⟨110⟩	⟨uvo⟩	⟨*uuw*⟩	[*uvw*]	
*m*3*m*	6_Rmm_R	$4mm1_R$	$2mm1_R$	2_Rmm_R	2_Rmm_R	2_R	
43*m*	3*m*	4_Rmm_R	$m1_R$	m_R	*m*	1	
432	$3m_R$	$4m_Rm_R$	$2m_Rm_R$	m_R	m_R	1	
Point group	⟨111⟩	⟨100⟩	⟨*uvo*⟩	[*uvw*]			
*m*3	6_R	$2mm1_R$	2_Rmm_R	2_R			
23	3	$2m_Rm_R$	m_R	1			
Point group	[0001]	$\langle 11\bar{2}0\rangle$	$\langle 1\bar{1}00\rangle$	[*uv.o*]	[*uu.w*]	$[u\bar{u}.w]$	[*uv.w*]
6/*mmm*	$6mm1_R$	$2mm1_R$	$2mm1_R$	2_Rmm_R	2_Rmm	2_Rmm_R	2_R
$\bar{6}m2$	$3m1_R$	$m1_R$	2*mm*	*m*	m_R	*m*	1
6*mm*	6*mm*	$m1_R$	$m1_R$	m_R	*m*	*m*	1
622	$6m_Rm_R$	$2m_Rm_R$	$2m_Rm_R$	m_R	m_R	m_R	1
Point group	[0001]	[*uv.o*]	[*uv.w*]				
6/*m*	61_R	2_Rmm_R	2_R				
$\bar{6}$	31_R	*m*	1				
6	6	m_R	1				
Point group	[0001]	$\langle 11\bar{2}0\rangle$	$[u\bar{u}.w]$	[*uv.w*]			
$\bar{3}m$	6_Rmm_R	21_R	2_Rmm_R	2_R			
3*m*	3*m*	1_R	*m*	1			
32	$3m_R$	2	m_R	1			
Point group	[0001]	[*uv.w*]					
$\bar{3}$	6_R	2_R					
3	3	1					
Point group	[001]	⟨100⟩	⟨110⟩	[*uow*]	[*uvo*]	[*uuw*]	[*uvw*]
4/*mmm*	$4mm1_R$	$2mm1_R$	$2mm1_R$	2_Rmm_R	2_Rmm_R	2_Rmm_R	2_R
$\bar{4}2m$	4_Rmm_R	$2m_Rm_R$	$m1_R$	m_R	m_R	*m*	1
4*mm*	4*mm*	$m1_R$	$m1_R$	*m*	m_R	*m*	1
422	$4m_Rm_R$	$2m_Rm_R$	$2m_Rm_R$	m_R	m_R	m_R	1
Point group	[001]	[*uvo*]	[*uvw*]				
4/*m*	41_R	2_Rmm_R	2_R				
$\bar{4}$	4_R	m_R	1				
4	4	m_R	1				
Point group	[001]	⟨100⟩	[*uow*]	[*uvo*]	[*uvw*]		
mmm	$2mm1_R$	$2mm1_R$	2_Rmm_R	2_Rmm_R	2_R		
*mm*2	2*mm*	$m1_R$	*m*	m_R	1		
222	$2m_Rm_R$	$2m_Rm_R$	m_R	m_R	1		
Point group	[010]	[*uow*]	[*uvw*]				
2/*m*	21_R	2_Rmm_R	2_R				
m	1_R	*m*	1				
2	2	m_R	1				
Point group	[*uvw*]						
$\bar{1}$	2_R						
1	1						

diffraction groups expected at all the possible zone axes for the 32 point groups. A flow chart for the point-group determination is given by Tanaka, Terauchi & Kaneyama (1988).

2.1.5. *Projection diffraction groups.* The effect of reflections of higher-order Laue zones (HOLZs) on the zeroth-order Laue-zone (ZOLZ) reflections takes place in two ways. The first results from the overlapping of dynamical Laue functions of HOLZ and ZOLZ reflections, giving non-sharp modulations to the intensities of the ZOLZ reflections. A measure of the amount of this effect is d/ξ_g, d and ξ_g being the lattice spacing and extinction distance of the HOLZ reflection concerned, respectively. Then, the effect becomes serious for strong HOLZ reflections when the distance between the HOLZ and ZOLZ is small but can be ignored for crystals with short (< 1 nm) lattice spacings along the incident-beam direction. The second is caused by the direct excitation of HOLZ reflections appearing as HOLZ rings outside the ZOLZ reflection disks and as sharp defect lines in ZOLZ disks. This effect is more important in usual cases. When these HOLZ reflections are weak and only ZOLZ reflections are observed, the symmetry elements of the specimen projected along the zone axis are determined from such CBED patterns. The projection of a specimen along a zone axis introduces a horizontal mirror symmetry. Ten projection diffraction groups are produced by adding a symmetry 1_R to the 31 diffraction groups, as shown in the last column of Table 3. When only ZOLZ reflections are observed in CBED patterns, two projection diffraction groups obtained from two different zone-axis settings are necessary to determine a crystal point group. It should be noted that if a diffraction group is identified carelessly from CBED patterns in which only ZOLZ reflections are observed, wrong point groups are deduced.

2.2. *Space-group determination*

2.2.1. *Identification of lattice types.* In the course of point-group determination, orientations of symmetry elements are determined with respect to diffraction patterns. On the basis of results, an integral-number index is given to each reflection spot in a diffraction pattern. The systematic absence of reflections makes clear the lattice type of a crystal. It should be noted that the reflections forbidden by lattice types are always absent even if dynamical diffraction takes place. By comparison of experimentally obtained absences and extinction rules given for lattice types [P, $C(A,B)$, I, F and R], a lattice type is identified for a crystal examined.

2.2.2. *Identification of screw axes and glide planes.* There are three space-group symmetry elements of diperiodic plane figures: (1) a horizontal screw axis $2_1'$; (2) a vertical glide plane g with a horizontal glide vector; and (3) a horizontal glide plane g'. These are related to point-group symmetry elements $2'$, m and m', respectively. From these elements, together with ten symmetry elements of the point groups, 80 space groups are produced.

Usual extinction rules for screw axes and glide planes hold only in the approximation of kinematical diffraction. Kinematically forbidden reflections caused by these symmetry elements appear owing to *Umweganregung* of dynamical diffraction; however, extinction of intensity still takes place in these reflections for certain crystal settings with respect to the incident beam. The dynamical extinction effect was first predicted by Cowley & Moodie (1959) and discussed by Miyake, Takagi & Fujimoto (1960) and Cowley, Moodie, Miyake, Takagi & Fujimoto (1961). Goodman & Lehmpfuhl (1964) first observed dynamical extinction as dark cross lines in kinematically forbidden reflection disks of CBED patterns of CdS. Gjønnes & Moodie (1965) developed a general theory of dynamical extinction between not only ZOLZ reflections but also HOLZ reflections. These extinction lines are the G–M lines.

Fig. 6(*a*) illustrates *Umweganregung* paths to a forbidden reflection. The $0k0$ (k = odd) reflections are kinematically forbidden owing to a b glide plane perpendicular to the a axis and/or a 2_1 screw axis in the b direction. Let us consider an *Umweganregung* path a in the zeroth Laue zone for the 010 forbidden reflection. Path b is geometrically equivalent to path a with respect to the glide plane and the 2_1 screw axis. Owing to a translation of one half of the lattice translation caused by the 2_1 screw axis and/or the glide plane, the following relations exist between the crystal structure factors.

$$\begin{aligned} F(h,k) &= F(\bar{h},k) \quad \text{for} \quad k = 2n, \\ F(h,k) &= -F(\bar{h},k) \quad \text{for} \quad k = 2n+1. \end{aligned} \tag{1}$$

That is, the structure factor of a reflection $hk0$ and that of a reflection $\bar{h}k0$ have the same phase for reflections of even order k but opposite phases for reflections of odd order k.

Since an *Umweganregung* path to a kinematically forbidden reflection $0k0$ (k = odd) contains an odd number of reflections with odd k, the following equations hold:

$$\begin{aligned} &F(h_1,k_1)F(h_2,k_2)\ldots F(h_n,k_n) \quad \text{for path } a \\ &= -F(\bar{h}_1,k_1)F(\bar{h}_2,k_2)\ldots F(\bar{h}_n,k_n) \quad \text{for path } b, \end{aligned} \tag{2}$$

where

$$\sum_{i=1}^{n} h_i = 0, \quad \sum_{i=1}^{n} k_i = k \quad (k = \text{odd})$$

and functions involving the excitation errors are omitted because we consider the cases where the functions are the same for all these paths. When the

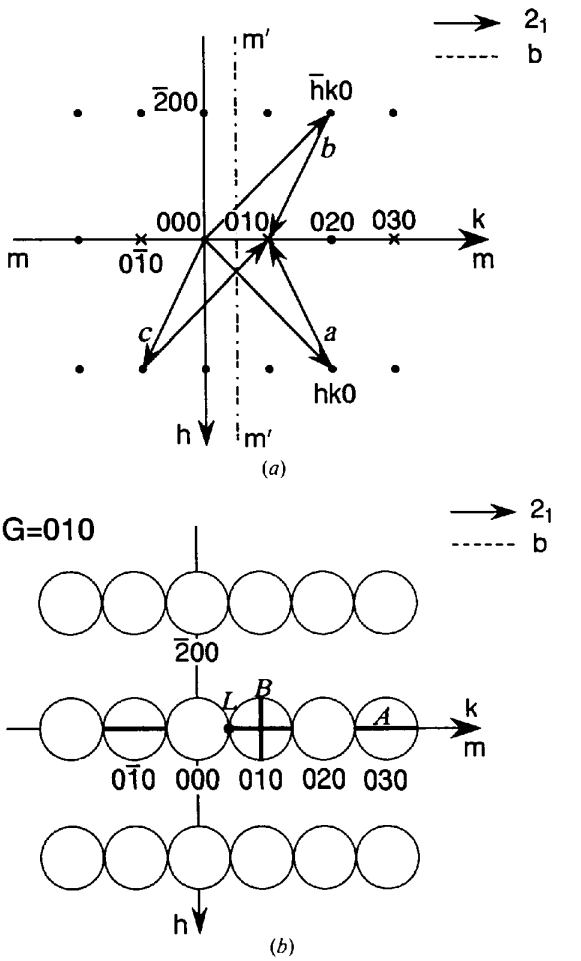

Fig. 6. Illustration of the production of G–M lines in kinematically forbidden reflections owing to a b glide plane and a 2_1 screw axis. (*a*) *Umweganregung* paths a, b and c. (*b*) A and B G–M lines in forbidden reflections. The first-order reflection is set at the Bragg condition.

Table 6. *Dynamical extinction rules for space-group symmetry elements g, g′ and 2′ of an infinitely extended parallel-sided specimen*

Symmetry elements of parallel-sided specimen	Orientation to specimen surface	GM lines	
		Two-dimensional (ZOLZ) interaction	Three-dimensional (HOLZ) interaction
Glide planes	Perpendicular: g	A_2 and B_2	A_3
	Parallel: g'	—	Intersection of A_3 and B_3
Twofold screw axes	Parallel: $2_1'$	A_2 and B_2	B_3

projection of the Laue point along the zone axis concerned lies on the axis k, the excitation errors between paths a and b are the same. Since the waves passing through paths a and b have the same amplitude but opposite signs, these two waves are superposed on the $0k0$ disks (k = odd) and cancel each other out, resulting in horizontal dark lines A in the forbidden disks, as shown in Fig. 6(b). The line A runs along the direction of the screw axis or the glide translation passing the zone axis of projection.

In path c, the reflections are arranged in reverse order compared with those in path b. When the 010 reflection is exactly excited, the two paths a and c are symmetric with respect to the bisector ($m'-m'$) of the 010 vector and have the same excitation error. The waves passing through these paths have the same amplitude but opposite signs. That is:

$$\begin{aligned} &F(h_1,k_1)F(h_2,k_2)\ldots F(h_n,k_n) && \text{for path } a \\ &= -F(\bar{h}_n,k_n)F(\bar{h}_{n-1},k_{n-1})\ldots F(\bar{h}_1,k_1) && \text{for path } c. \end{aligned} \quad (3)$$

As a result, these two waves cancel each other out on the 010 disk, resulting in a vertical dark line B in this disk, also shown in Fig. 6(b). The line B occurs perpendicular to the line A along the exact Bragg positions. When *Umweganregung* paths are present only in the zeroth Laue zone, the glide plane and screw axis produce the same dynamical extinction lines A and B. We call these lines A_2 and B_2 G–M lines, the subscript 2 indicating two-dimensional interaction.

The dynamical extinction effect is analogous to the interference phenomenon in the Michelson interferometer; that is, the incident beam is split into two beams by Bragg reflections in a crystal. These beams run along different *Umweganregung* paths, in which they suffer a relative phase shift of π when reflected by crystal planes and are then superposed on a kinematically forbidden reflection to cancel each other out.

When the paths take in higher-order Laue zones, the glide plane produces only G–M lines A but the screw axis causes only G–M lines B. These facts are attributed to the different relations between structure factors for a 2_1 screw axis and a glide plane.

$$F(hkl) = (-1)^k F(\bar{h}k\bar{l}) \quad \text{for a } 2_1 \text{ screw axis,} \quad (4)$$

$$F(hkl) = (-1)^k F(\bar{h}kl) \quad \text{for a glide plane.} \quad (5)$$

In the case of the glide plane, two waves passing through paths a and b have opposite signs to each other according to the lower equation and form G–M lines A, but G–M lines B are not produced because the upper equation holds only for the 2_1 screw axis. In the case of the 2_1 screw axis, only the waves passing through paths a and c have opposite signs according to the upper equation, forming G–M lines B only. We call these lines A_3 and B_3 G–M lines, the suffix 3 indicating three-dimensional interaction. It was predicted by Gjønnes & Moodie (1965) that a horizontal glide plane g' would give a dark spot at the crossing point between lines A and B in Fig. 6(b), owing to the cancellation between waves passing through paths b and c. Dynamical extinction caused by a g', which showed a little difference from the prediction, was observed for spinel and silicon (Tanaka, Terauchi & Sekii, 1987). Table 6 shows G–M line rules for glide planes g and g' and a $2_1'$ screw axis. Since the three space-group symmetry elements give different dynamical extinctions, these elements can be identified from observed extinctions.

A horizontal screw axis and vertical glide plane can be identified by observation of three-dimensional G–M lines A_3 and B_3. It is not, however, easy to observe three-dimensional G–M lines because of the simultaneous presence of broad two-dimensional G–M lines. The presence of three-dimensional G–M lines can be revealed by inspection of the symmetries of fine-defect HOLZ lines in forbidden reflections in place of direct observation of the G–M lines (Tanaka, Saito & Sekii, 1983). That is, if HOLZ lines form three-dimensional G–M lines, the HOLZ lines are symmetric with respect to two-dimensional G–M lines and *vice versa*. When HOLZ lines are symmetric about A_2 G–M lines, the specimen crystal has a glide plane. When HOLZ lines are symmetric with respect to B_2 G–M lines, a 2_1 screw axis exists. It should be noted that HOLZ lines in ZOLZ reflection disks become clearly visible when relatively thick areas of a crystal are examined.

Fig. 7 shows CBED patterns taken at the 010 Bragg setting from (a) thin and (b) thick areas of FeS_2, whose space group is $P2_1/a\bar{3}$, with [001] electron incidence. In the odd-order disks of Fig. 7(a), broad G–M lines owing to two-dimensional interaction are seen. On the other hand, the fine HOLZ

lines owing to three-dimensional interaction are clearly seen in Fig. 7(*b*). The HOLZ lines are symmetric with respect to both A_2 and B_2 G–M lines in the 010 disk. This fact proves the presence of A_3 and B_3 G–M lines, or the presence of a glide plane and a 2_1 screw axis, showing good agreement with the space group of FeS_2.

Another practical method to distinguish between glide planes and 2_1 screw axes is that reported by Steeds, Rackham & Shannon (1978). The method is based on the fact that G–M lines are observable even when a crystal is rotated with a glide plane and 2_1 screw axis kept parallel and perpendicular to the incident beam, respectively. With reference to Fig. 6(*a*), A_3 G–M lines produced by a glide plane remain even when the crystal is rotated with respect to axis h but all the G–M lines are destroyed by a rotation of the crystal about axis k. B_3 G–M lines originating from a 2_1 screw axis are not destroyed by a crystal rotation about axis k but all the G–M lines are destroyed by a rotation with respect to axis h.

2.2.3. *Space-group determination.* We describe a space-group-determination method using G–M lines caused by symmetry elements $2_1'$ and g of an infinitely extended parallel-sided specimen because extinction owing to horizontal glide planes g' has less practical importance. To be precise, a vertical glide plane with a glide vector that is not parallel to the surface cannot be a symmetry element of a specimen of finite thickness. The components of the translation vectors perpendicular to the incident beam, however, act as a symmetry element g. The 2_1, 4_1, 4_3, 6_1, 6_3 and 6_5 screw axes of crystal space groups that are set perpendicular to the incident beam act as a symmetry element $2_1'$ because two or three successive operations of 4_1, 4_3, 6_1, 6_3 and 6_5 screw axes make them equivalent to a 2_1 screw axis: $(4_1)^2 = (4_3)^2 = (6_1)^3 = (6_3)^3 = (6_5)^3 = 2_1$. The 4_2, 3_1, 3_2, 6_2 and 6_4 screw axes that are set perpendicular to the incident beam do not produce G–M lines because a 4_2 axis acts as a twofold axis owing to the relation $(4_2)^2 = 2$. In addition, horizontal threefold screw axes give no symmetry in CBED patterns and 6_2 and 6_4 screw axes are equivalent to 3_2 and 3_1 owing to the relations $(6_2)^2 = 3_2$ and $(6_4)^2 = 3_1$.

The modification of G–M line rules, given in Table 6, when several crystal symmetry elements, which give rise to G–M lines, coexist and when the symmetry elements are combined with various lattice types (Tanaka, Sekii & Nagasawa, 1983), was investigated. Using the results, G–M lines A_2, A_3, B_2 and B_3 expected from all the possible crystal settings for all the space groups are tabulated (Tanaka, Sekii & Nagasawa, 1983; Tanaka & Terauchi, 1985). From the tables, it was found that 181 space groups out of 230 can be identified using G–M lines.

49 crystal space groups that cannot be identified by G–M lines are listed in Table 7. Most of the indistinguishable sets are caused by the fact that CBED cannot identify 4_2, $3_1(3_2)$ and $6_2(6_4)$ screw axes. These sets can most easily be distinguished by orienting the crystal to obtain, as near as possible, the systematic reflection 00*l* row (with the c axis parallel to the screw axis) only. The absence of strong *Umweganregung* paths, present in a two-dimensional pattern, then ensures that the kinematically forbidden reflections will be absent or extremely weak. With this test, each of a space-group pair can be identified except the pairs in parentheses in Table 7. These pairs form left- and right-handed space groups. The handedness of space groups was identified for quartz by Goodman & Secomb (1977) and

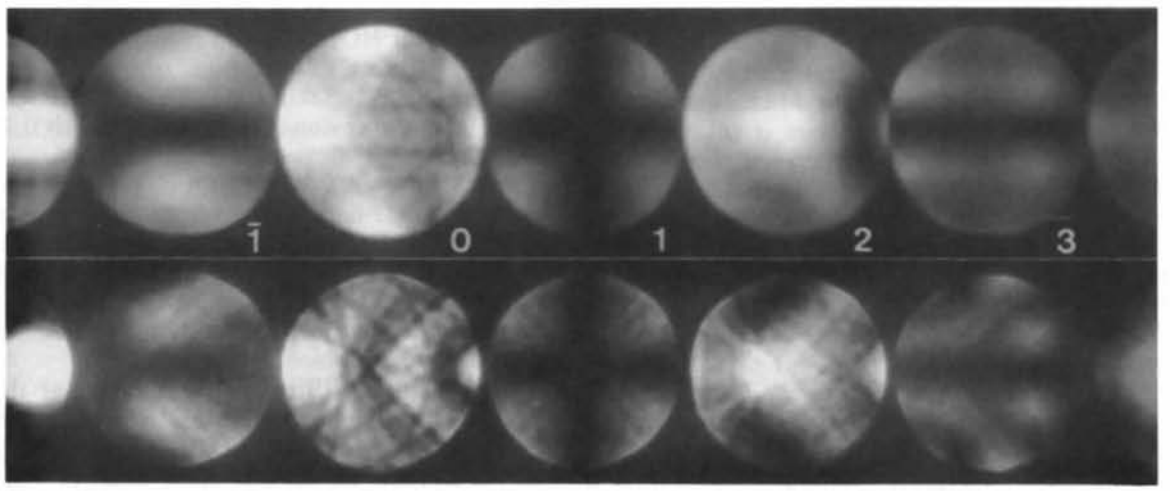

Fig. 7. CBED patterns obtained from (*a*) thin and (*b*) thick areas of a (001) FeS_2 film. (*a*) A_2 and B_2 G–M lines are seen. (*b*) HOLZ lines symmetric with respect to A_2 and B_2 G–M lines show the presence of A_3 and B_3 G–M lines.

Table 7. *Crystal space groups indistinguishable by G–M lines*

1. $P3$, ($P3_1$, $P3_2$)	12. $P422$, $P4_222$
2. $P312$, ($P3_112$, $P3_212$)	13. $P42_12$, $P4_22_12$
3. $P321$, ($P3_121$, $P3_221$)	14. $I4$, $I4_1$
4. $P6$, ($P6_2$, $P6_4$)	15. $I422$, $I4_122$
5. $P622$, ($P6_222$, $P6_422$)	16. $I23$, $I2_13$
6. $P6_3$, ($P6_1$, $P6_5$)	17. $I222$, $I2_12_12_1$
7. $P6_322$, ($P6_122$, $P6_522$)	18. $P432$, $P4_232$
8. $P4$, $P4_2$	19. ($P4_132$, $P4_332$)
9. ($P4_1$, $P4_3$)	20. $I432$, $I4_132$
10. $P4/m$, $P4_2/m$	21. $F432$, $F4_132$
11. $P4/n$, $P4_2/n$	

Goodman & Johnson (1977) and for MnSi by Tanaka, Takayoshi, Ishida & Endoh (1985). The senses of two crystal axes were determined with the aid of kinematical structure-factor calculations and the sense of the third crystal axis was determined with the aid of dynamical calculations. It should be noted that two special pairs ($I222$ and $I2_12_12_1$, and $I23$ and $I2_13$) cannot be distinguished from kinematical extinction rules but can be distinguished when atomic positions are determined. Therefore, it is not necessary to distinguish between these two sets of space groups when identifying a space group. A flow chart of the space-group determination is shown by Tanaka, Terauchi & Kaneyama (1988). Similar but different procedures for crystal point- and space-group determination have been given by Steeds & Vincent (1983) and Goodman (1984).

Space-group determination as described above is carried out using *G–M* lines appearing in ZOLZ reflections. Vertical glide planes whose translation vectors are perpendicular to the specimen surface do not cause *G–M* lines in ZOLZ reflections but cause them in HOLZ reflections; there, they are called '*A*' *G–M* lines. Vertical glide planes whose translation vectors have vertical components also cause *G–M* lines. It should be noted that vertical glide planes with glide translations not parallel to the surface are not symmetry elements of diperiodic plane figures. Vertical screw axes are expected to form *G–M* lines in HOLZ reflections whose vectors are parallel to the screw axes; however, these reflections cannot be observed by usual transmission CBED. Therefore, only these glide planes can be identified from *G–M* lines in HOLZ reflections.

Tables of *G–M* lines appearing in HOLZ reflections at various incident-beam orientations for all the space groups that have glide planes are given by Tanaka, Terauchi & Kaneyama (1988). Simultaneous examination of ZOLZ and HOLZ *G–M* lines enables quicker and easier identification of crystal space groups. It has been shown that CBED does not necessarily observe the space-group elements of diperiodic plane figures. Then, to give the relation between the space groups of crystals and those of diperiodic plane figures is of no importance. It must be emphasized that CBED observes the point- and space-group symmetry elements of crystals. Discussions of symmetry elements observed by CBED and the details of symmetry determination are given by Tanaka, Terauchi & Kaneyama (1988) and Tanaka (1989).

2.3. *Example*

We demonstrate the point- and space-group-determination procedures using $La_2CuO_{4-\delta}$ as an example. $La_{2-x}M_xCuO_{4-\delta}$ (M = Ba, Sr and Ca) is a 40 K class superconductor. Many space groups were proposed for this system: *Fmmm*, *Fmm*2, *F*222 and *Cmmm* (or *C*222) for $La_{2-x}Sr_xCuO_{4-\delta}$; *Cmca*, *Pccn* and *Cmmm* for $La_{2-x}Ba_xCuO_{4-\delta}$; *Cmca*, *Pccn* and *Cmmm* for $La_2CuO_{4-\delta}$. These controversial results were attributed to specimen preparation, doping effects and experimental accuracy. Intensity profile fits obtained by the Rietveld method for the neutron powder diffraction data from as-grown $La_2CuO_{4-\delta}$ were excellent but showed no difference for the two space groups, *Cmca* and *Pccn*. Therefore, the space groups could not be distinguished from the powder diffraction data.

The substance was already known to belong to the orthorhombic system with the lattice parameters a = 5.3548, b = 5.4006 and c = 13.1592 Å. Fig. 8(*a*) shows a CBED pattern taken at [001] incidence, Fig. 8(*b*) being the central part of Fig. 8(*a*). The whole pattern has symmetry 2*mm*. This indicates that the crystal has two mirror symmetries perpendicular to each other and that the point group is *mmm* or *mm*2. To investigate whether the third mirror plane perpendicular to these two mirror exists or not, a CBED pattern was taken at [100] incidence [Fig. 9(*a*), of which Fig. 9(*b*) shows the central part]. Two mirror planes are seen, of which one is the third one. As a result, the point group was determined to be *mmm*.

Ordinary electron diffraction patterns revealed the lattice type to be *B* centered. Fig. 9(*c*) was taken by tilting the incident beam in the b^* direction from the [100] zone axis to clearly observe the *G–M* lines. A_2 *G–M* lines are seen in the 010 and $0\bar{5}0$ reflections. Reference to Table 8 for ZOLZ *G–M* lines clarifies that the possible space groups are *Bmab* and *Bmmb*. Table 8 indicates that we can distinguish two space groups if we examine whether *G–M* lines appear in h_o0l_o reflections at a [$u0w$] incidence; however, an examination at a low-symmetry incidence must also be conducted but may be troublesome. Further examinations are possible at high-symmetry incidences, when HOLZ *G–M* lines are utilized. Table 9 shows that two space groups can be distinguished when it is examined whether *A G–M* lines appear in h_o0l_o HOLZ reflections at the [100] incidence. Since a CBED pattern at this incidence has already been

taken, no new experiment is necessary. In Fig. 9(*a*), *A G–M* lines are seen in the 10*l* and 10$\bar{l}$ HOLZ reflections. Therefore, the space group was determined to be *Bmab*, which is equivalent to the standard notation *Cmca*.

3. Symmetry determination of four-dimensional crystals – incommensurate crystals

3.1. *CBED symmetries from incommensurate crystals*

It was shown by de Wolff (1974, 1977) that a one-dimensional displacively and substitutionally modulated crystal can be described as a three-dimensional section of a four-dimensional (periodic) crystal. Janner & Janssen (1980) developed a more general approach to describe the modulated crystals with n modulations as the $(3+n)$-dimensional (periodic) crystals ($n=1, 2, ...$). A. Yamamoto (1982) derived a general structure-factor formula for the n-dimensionally modulated crystal ($n=1, 2, ...$), which holds for both displacively and substitutionally modulated crystals. The tables of the four-dimensional space groups for one-dimensional incommensurately modulated crystals were given by de Wolff, Janssen & Janner (1981). Later, some corrections of the tables were reported by Yamamoto, Janssen, Janner & de Wolff (1985).

We are concerned here only with displacively modulated crystals. Fig. 10(*a*) illustrates the four-dimensional description of a one-dimensional displacively modulated structure. The arrows labeled a_1–a_4 indicate the four-dimensional crystal axes. The horizontal line labeled R_3 represents the three-dimensional space (real world). In the four-dimensional description, an atom is not located at a point as in three-dimensional space but is expressed by a string, which extends along the fourth direction a_4 perpendicular to the three-dimensional space R_3. The parallelogram drawn with a thick line is a unit cell in the four-dimensional space. The unit cell contains two atom strings. The wavy shape of the atom strings, which are periodic along a_4, represents

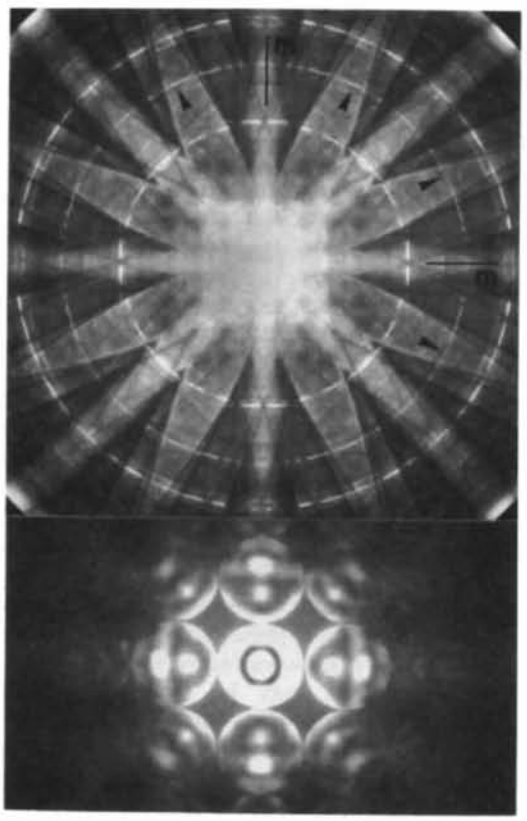

Fig. 8. (*a*) CBED pattern of $La_2CuO_{4-\delta}$ taken at [001] incidence; (*b*) the central part of (*a*).

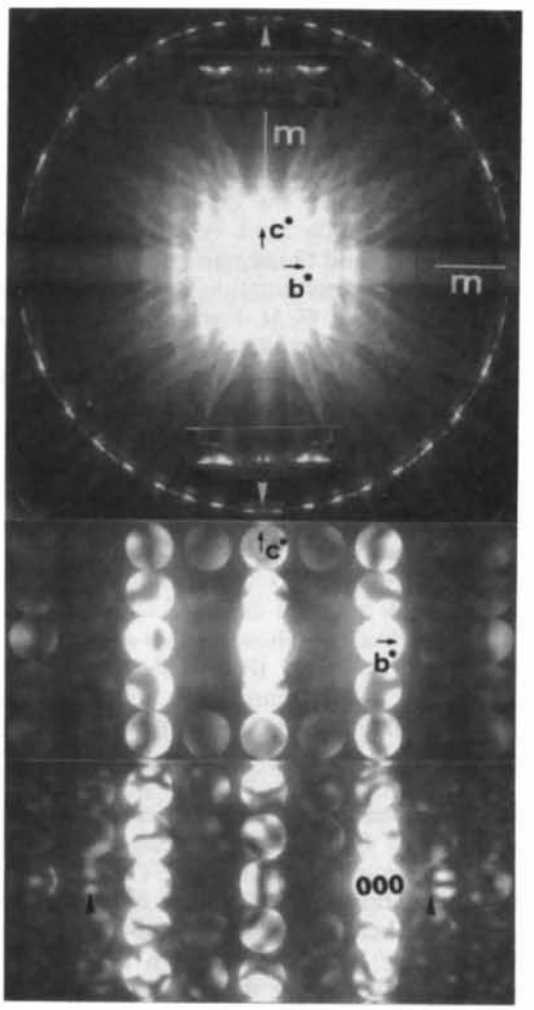

Fig. 9. (*a*) CBED pattern of $La_2CuO_{4-\delta}$ taken at [100] incidence; (*b*) the central part of (*a*); (*c*) pattern produced by slightly tilting the incidence in the b^* direction.

Table 8. *ZOLZ G–M line table for space groups nos.* 63–68

Incident beam direction / Space group	[100]		[010]		[001]		[uv0]		[0vw]		[u0w]	
63 $B2/m2_1/m2/b$	$0k_o0$ $b,2_1$	$A_2\,B_2$ $A_3\,B_3$			$0k_o0$ 2_1	B_3	h_ek_o0 b	$A_2\,B_2$ A_3			$0k_o0$ 2_1	$A_2\,B_3$ B_3
64 $B2/m2_1/a2/b$	$0k_o0$ $b,2_1$	$A_2\,B_2$ $A_3\,B_3$			$0k_o0$ 2_1	B_3	h_ek_o0 b	$A_2\,B_2$ A_3			h_o0l_o a $0k_o0$ 2_1	$A_2\,B_2$ A_3 $A_2\,B_2$ B_3
65 $B2/m2/m2/m$												
66 $B2/b2/m2/b$	$0k_o0$ b_2	A_3			$0k_o0$ b_1	A_3	h_ek_o0 b_2	$A_2\,B_2$ A_3	$0k_ol_e$ b_1	$A_2\,B_2$ A_3		
67 $B2/m2/a2/m$											h_o0l_o a	$A_2\,B_2$ A_3
68 $B2/b2/a2/b$	$0k_o0$ b_2	A_3			$0k_o0$ b_1	A_3	h_ek_o0 b_2	$A_2\,B_2$ A_3	$0k_ol_e$ b_1	$A_2\,B_2$ A_3	h_o0l_o a	$A_2\,B_2$ A_3

Table 9. *HOLZ G–M line table for space groups nos.* 63–68

Incident beam direction / Space group	[100]		[010]		[001]		[uv0]		[0vw]		[u0w]	
63 $B2/m2_1/m2/b$	h_ek_o0 b	A	h_ek_o0 b	A			h_ek_o0 b	A_h				
64 $B2/m2_1/a2/b$	h_ek_o0 b h_o0l_o a	A	h_ek_o0 b	A	h_o0l_o a	A	h_ek_o0 b	A_h			h_o0l_o a	A_h
65 $B2/m2/m2/m$												
66 $B2/b2/m2/b$	h_ek_o0 b_{23}	A	$0k_ol_e$ b_{11} h_ek_o0 b_{23}	A	$0k_ol_e$ b_{11}	A	h_ek_o0 b_{23}	A_h	$0k_ol_e$ b_{11}	A_h		
67 $B2/m2/a2/m$	h_o0l_o a	A			h_o0l_o a	A					h_o0l_o a	A_h
68 $B2/b2/a2/b$	h_ek_o0 b_{23} h_o0l_o a	A	$0k_ol_e$ b_{11} h_ek_o0 b_{23}	A	h_o0l_o a $0k_ol_e$ b_{11}	A	h_ek_o0 b_{23}	A_h	$0k_ol_e$ b_{11}	A_h	h_o0l_o a	A_h

a displacive-type modulation. The width of the atom strings indicates the spread of the atom in R_3. The atom positions of the modulated structures in R_3 are given as a three-dimensional section of the atom strings in the four-dimensional space. The diffraction vector **G** is written as

$$\mathbf{G} = h_1\mathbf{a}^* + h_2\mathbf{b}^* + h_3\mathbf{c}^* + h_4\mathbf{k},$$

where a set of $h_1h_2h_3h_4$ is a four-dimensional reflection index and $\mathbf{a}^*$, $\mathbf{b}^*$ and $\mathbf{c}^*$ are the reciprocal-lattice vectors of the real-lattice vectors **a**, **b** and **c** of the average structure. The modulation wave vector **k** is written as

$$\mathbf{k} = k_1\mathbf{a}^* + k_2\mathbf{b}^* + k_3\mathbf{c}^*,$$

where one coefficient of $k_i (i = 1\text{–}3)$ is an irrational number and the others are rational. The structure factor $F(h_1h_2h_3h_4)$ for the four-dimensional crystal is given by de Wolff (1974, 1977) as follows.

$$F(h_1h_2h_3h_4) = \sum_{\mu=1}^{N} f_\mu \exp 2\pi i(h_1\overline{x_1^\mu} + h_2\overline{x_2^\mu} + h_3\overline{x_3^\mu}) \times \int_0^1 \exp 2\pi i\Big[\sum_{i=1}^{3}(h_i + h_4k_i)u_i^\mu + h_4\overline{x_4^\mu}\Big]\mathrm{d}\overline{x_4^\mu}, \quad (6)$$

where $\overline{x_4^\mu} = (\overline{x_1^\mu} + n_1)k_1 + (\overline{x_2^\mu} + n_2)k_2 + (\overline{x_3^\mu} + n_3)k_3$. The symbols f_μ and $\overline{x_i^\mu} (i = 1\text{–}3)$ are the atom form

factor and the ith component of the position of the μth atom in the unit cell of the average structure, respectively. The symbol u_i^μ is the ith component of the displacement from the atom position $\overline{x_i^\mu}$ of the μth atom. Since the atom in the four-dimensional space is continuous along a_4 and discrete along R_3, the structure factor is expressed by the summation in R_3 and the integration along a_4. A three-dimensional section of the four-dimensional unit cell gives a modulated atomic arrangement at a unit cell of the average structure in R_3. Then, the atom strings in the four-dimensional unit cell correspond to the sum of the atom displacements over an infinite number of unit cells of the average structure. This means that (6) is the structure factor for the unit cell with the lattice parameter of an infinite length in R_3 along the direction of the modulation wave vector $\mathbf{k}$.

For simplicity, we assume that the modulation wave vector is written as $\mathbf{k} = \mathbf{k}_3\mathbf{c}^*$ and the modulated structure belongs to the four-dimensional space group $P^{P2/m}_{\ 1\ 1}$. This space-group symbol indicates that: (i) the modulation wave vector k exists inside the first Brillouin zone for the average structure (P); (ii) the average structure belongs to the space group $P2/m$; (iii) the modulated structure has a twofold rotation axis, which is common to both the average and modulated structures (subsymbol 1), but does not have the mirror symmetry possessed by the average structure (subsymbol $\bar{1}$). For the twofold rotation axis of this four-dimensional space group, the structure factor $F(h_1h_2h_3h_4)$ [(6)] is written as

$$\begin{aligned} F(h_1h_2h_3h_4) = &\sum_{\mu=1}^{N} f_\mu \exp 2\pi i(h_1\overline{x_1^\mu} + h_2\overline{x_2^\mu} + h_3\overline{x_3^\mu}) \\ &\times\left\{\int_0^1 \exp 2\pi i[h_1u_1^\mu + h_2u_2^\mu \right. \\ &\left. + (h_3 + h_4k_3)u_3^\mu + h_4\overline{x_4^\mu}]\mathrm{d}\overline{x_4^\mu}\right\} \\ &+ \sum_{\mu=1}^{N} f_\mu \exp 2\pi i(-h_1\overline{x_1^\mu} - h_2\overline{x_2^\mu} + h_3\overline{x_3^\mu}) \\ &\times\left\{\int_0^1 \exp 2\pi i[-h_1u_1^\mu - h_2u_2^\mu \right. \\ &\left. + (h_3 + h_4k_3)u_3^\mu + h_4\overline{x_4^\mu}]\mathrm{d}\overline{x_4^\mu}\right\}, \end{aligned} \tag{7}$$

where $\overline{x_4^\mu} = (\overline{x_3^\mu} + n_3)k_3$. We consider the reflections $h_1h_2h_3h_4$ and $\bar{h}_1\bar{h}_2h_3h_4$, which are equivalent with respect to the twofold rotation axis of the average structure. The symmetry subsymbol 1, which is written beneath symmetry symbol 2 in the expression for the four-dimensional space group, indicates that the modulation wave vector $\mathbf{k}$ is transformed into itself by symmetry operation 2 of the average structure. It is clear from (7) that the structure factor $F(\bar{h}_1\bar{h}_2h_3h_4)$ is equal to the structure factor $F(h_1h_2h_3h_4)$. Hence, the intensities of the $h_1h_2h_3h_4$ and $\bar{h}_1\bar{h}_2h_3h_4$ reflections are equal. It is clarified that the symmetry of the reflections ($h_4 \neq 0$) due to the modulated structure (incommensurate reflections) is the same as that of the fundamental reflections ($h_4 = 0$) due to the average structure with respect to the twofold rotation axis of the average structure.

Next, we consider the reflections $h_1h_2h_3h_4$ and $h_1h_2\bar{h}_3\bar{h}_4$, which are equivalent with respect to the mirror symmetry of the average structure. The symmetry subsymbol $\bar{1}$, which is written beneath symmetry symbol m in the expression for the four-dimensional space group, indicates that the modulation wave vector $\mathbf{k}$ is transformed into $-\mathbf{k}$ by the symmetry operation m. For the incommensurate reflections ($h_4 \neq 0$), the formulas corresponding to the terms within curly brackets of $F(h_1h_2h_3h_4)$ in (7) are not equal to those of $F(h_1h_2\bar{h}_3\bar{h}_4)$ because k_3 is an irrational number. Hence, the intensity of the $h_1h_2h_3h_4$ reflection is not equal to that of the $h_1h_2\bar{h}_3\bar{h}_4$ reflection. For the fundamental reflections ($h_4 = 0$), the intensity of the $h_1h_2h_30$ reflection is equal to that of the $h_1h_2\bar{h}_30$ reflection because $F(h_1h_2h_30)$ is equal to $F(h_1h_2\bar{h}_30)$. It should be noted that this mirror symmetry m between the fundamental reflections is expected to be destroyed by the dynamical diffraction effect between the fundamental and incommensurate reflections. In most modulated structures, however, the amplitude of the modulation wave u_i^μ is not so large as to affect the symmetry of the fundamental reflections. Therefore, the fundamental reflections should show the symmetry of the average structure, while the incommensurate reflections lose this symmetry. The results obtained are summarized in the following rules.

(1) For symmetry subsymbol 1, both fundamental and incommensurate reflections show the symmetries of the average structure.

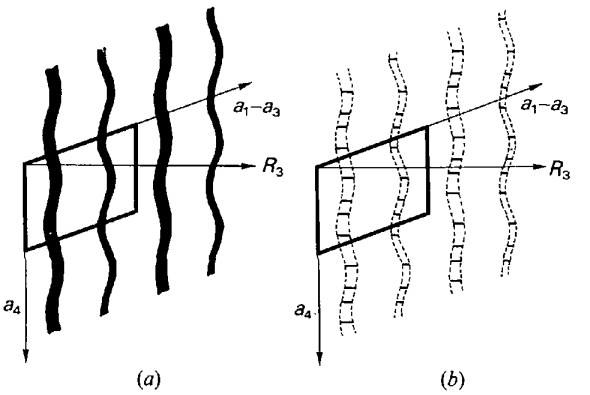

Fig. 10. Four-dimensional description of a one-dimensional displacively modulated crystal. The wavy strings are the four-dimensional atoms with a displacive modulation. (*a*) An infinite crystal, atoms being continuous in the a_4 direction. (*b*) A finite-volume crystal, atoms being expressed by three-dimensional sections with a finite number.

(2) For symmetry subsymbol $\bar{1}$, the fundamental reflections, in practice, show the symmetries of the average structure but the incommensurate reflections do not have any symmetries.

Rule (1) also holds for the symmetry subsymbols *s*, *t*, *q* and *h* of the four-dimensional space groups because those space-group symbols are expressed by subsymbol 1 in the frame of the four-dimensional point groups.

Real CBED patterns are obtained from a finite area of a crystal. A modulated structure with a finite volume in R_3 is expressed by a finite number of three-dimensional sections of atom strings in the four-dimensional unit cell, as shown in Fig. 10(*b*). Hence, it is necessary to use the structure factor which takes account of the effect of the finite size. The effect was clarified in detail by Terauchi & Tanaka (1993). The results obtained are summarized as follows.

(*a*) The four-dimensional symmetries can appear in CBED patterns if the patterns are taken from a specimen volume that contains more than one unit cell of the average structure. In other words, to obtain the symmetries expected from the four-dimensional symmetry symbols, it is not necessary to take the CBED pattern from such a specimen area whose diameter is larger than the approximate period of the modulated structure (the approximate least common multiple between the modulation wavelength and the unit-cell length of the average structure).

(*b*) Even if the size and the position of an illuminated specimen area are changed, the intensity distribution in the CBED pattern changes but the symmetry of the pattern does not change.

It is worthwhile to note the following facts. If the point-group symmetry of the average structure and the modulation wave vector **k** are completely known, the four-dimensional point groups themselves are determined by inspection of only how the modulation wave vector **k** is transformed by the symmetry operations of the average structure, although the symmetries of incommensurate reflections provide important information for the confirmation of the point groups. From this, it is seen that correct determination of the point-group symmetry of the average structure is very important in the determination of the four-dimensional point groups. Then, there is no doubt that the point groups of the average structure can be determined unambiguously by the CBED method when the amplitude of the modulation wave u_i^μ is not so large as to affect the symmetry of the fundamental reflections.

Terauchi & Tanaka (1993) also studied the case of substitutionally modulated crystals and clarified that rules (1) and (2) given above hold for this case, although a large enough volume to give the average atom form factor has to be illuminated.

Terauchi, Takahashi & Tanaka (1994) have shown theoretically that dynamical extinction occurs for the screw axes and glide planes of the incommensurately modulated crystal, which has an infinite dimension along the direction of the incommensurate modulation wave vector. They have also shown that approximate dynamical extinction can occur in the CBED patterns obtained from a finite specimen volume of the four-dimensional crystal. The tables of the dynamical extinction lines appearing in CBED patterns have been given by them for all the four-dimensional space groups. They have observed dynamical extinction in kinematically forbidden incommensurate reflections from $Sr_2Nb_2O_7$.

3.2. *Example*

Many materials of the $A_2B_2O_7$ family undergo phase transformations from the space group *Cmcm* to $Cmc2_1$ to $P2_1$ with decreasing temperatures. The phase transformation from *Cmcm* to $Cmc2_1$ has been reported to occur as a result of the rotation of the oxygen octahedra about the *a* axis with a slight deformation of the octahedra. The transformation from $Cmc2_1$ to $P2_1$ has been considered to be caused by rotation of the octahedra about the *b* axis. An incommensurate phase appears, for example, in $La_2Ti_2O_7$ (Tanaka, Sekii & Ohi, 1985) between the phase with space group $Cmc2_1$ and that with $P2_1$. $Sr_2Nb_2O_7$ transforms from the phase with $Cmc2_1$ into an incommensurate phase at 488 K but does not transform into the phase with $P2_1$. No discommensuration has been observed even at lower temperatures in the incommensurate phase. It was reported by N. Yamamoto (1982) and Yamamoto & Ishizuka (1983) that the modulated structures in this phase can be explained by the rotation of the oxygen octahedra about the *b* axis.

The incommensurate phase has a modulation wave vector $\mathbf{k} = (\frac{1}{2} - \delta)\mathbf{a}^*$ ($\delta = 0.009$–0.023). The symmetry of the incommensurately modulated structure of $Sr_2Nb_2O_7$ is expressed by the four-dimensional space group $P^{Cmc2_1}_{1\,s\,1}$ (Yamamoto, 1988). Then, the four-dimensional point group of the structure is written as $^{mm2}_{1\,1}$. The symbol implies the following substance. The modulation wave vector **k** is transformed to $-\mathbf{k}$ by a mirror symmetry operation perpendicular to the *a* axis ($^m_1$) and by the twofold rotation-symmetry operation along the *c* axis ($^2_1$). The wave vector is transformed into itself by the mirror symmetry perpendicular to the *b* axis ($^m_1$).

The experiments have been carried out with an electron probe about 3 nm in diameter. It should be noted that the probe size was smaller than the approximate period of the modulated structure – about 40 nm for $Sr_2Nb_2O_7$.

Fig. 11 shows a CBED pattern of the incommensurate phase of $Sr_2Nb_2O_7$ obtained with the [010]

incidence at an accelerating voltage of 60 kV. The reflections indicated by arrows are incommensurate reflections owing to the modulation. Other reflections are fundamental reflections owing to the average structure. The four-dimensional point-group symmetries ($^{m}_{1}$) about the a axis and ($^{2}_{1}$) about the c axis appear in this CBED pattern. When rule (2) of § 3.1 is considered, symmetry ($^{m}_{1}$) exhibits mirror symmetry perpendicular to the a axis between the fundamental reflections but no mirror symmetry between the incommensurate reflections. The same symmetries are expected from symmetry ($^{2}_{1}$) in the framework of the projected potential approximation. Fig. 11 shows these symmetries exactly.

Fig. 12 shows a CBED pattern of the incommensurate phase obtained with [201] incidence at an accelerating voltage of 60 kV. The reflections in two rows indicated by arrows are the incommensurate reflections. The other reflections are fundamental ones. The four-dimensional point-group symmetry about the b axis ($^{m}_{1}$) appears in this pattern. With reference to rule (1) of § 3.1, symmetry ($^{m}_{1}$) displays mirror symmetry perpendicular to the b axis not only between the fundamental reflections but also between the incommensurate reflections. Fig. 12 clearly shows the mirror symmetry between both kinds of reflections. Fig. 13 shows a CBED pattern obtained with the same incidence as in Fig. 12 but from a slightly different specimen area with nearly the same specimen thickness. The pattern shows the same symmetry as in Fig. 12 but the intensity distribution is different. This confirms result (b) described in § 3.1.

The space-group symbol imlies that the modulated structure has four-dimensional glide planes ($^{c}_{s}$) perpendicular to the b axis with a shift of $\frac{1}{2}c + \frac{1}{2}a_4$. Then, the reflections with $h_3 + h_4 = 2n + 1$ are kinematically forbidden. Fig. 14(a) shows an electron diffraction pattern obtained with [001] incidence at an accelerating voltage of 60 kV. The reflections in four columns indicated by black arrows are incommensurate reflections owing to the modulation. The reflections 0001, 000$\bar{1}$, 200$\bar{1}$ and $\bar{2}$001 indicated by white arrows are kinematically forbidden but have intensities owing to multiple diffraction. Other reflections are fundamental reflections owing to the average struc-

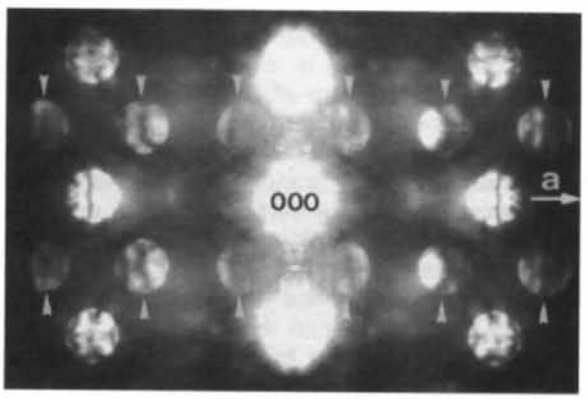

Fig. 11. CBED pattern of the incommensurate phase of $Sr_2Nb_2O_7$ taken with [010] incidence at an accelerating voltage of 60 kV. The reflections with arrows are incommensurate reflections owing to the modulation and the others are fundamental ones owing to the average structure. The latter reflections show mirror symmetry perpendicular to the a axis; the former do not.

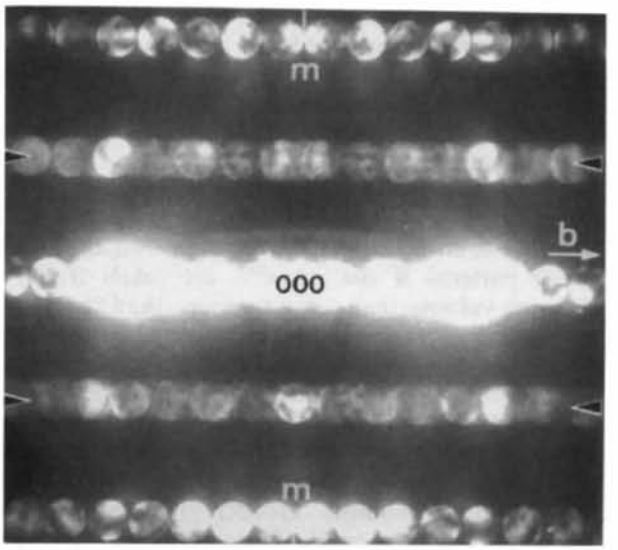

Fig. 12. CBED pattern of the incommensurate phase of $Sr_2Nb_2O_7$ taken with [201] incidence at 60 kV. The reflections at two levels indicated by arrows are the incommensurate ones; the others are fundamental ones. Both the fundamental and incommensurate reflections show mirror symmetry perpendicular to the b axis.

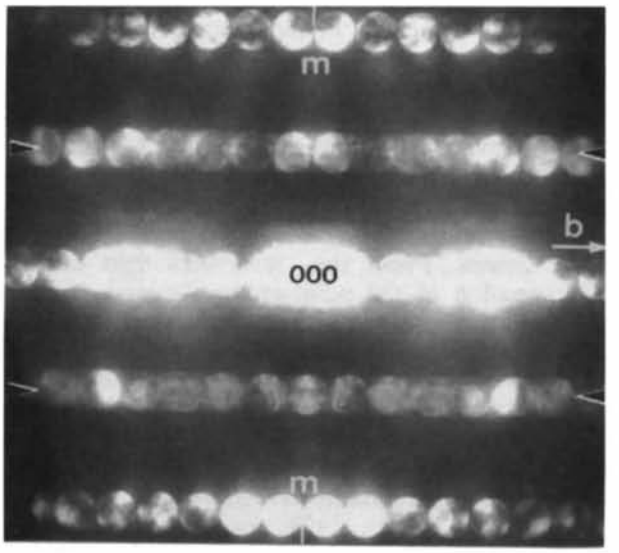

Fig. 13. CBED pattern of the incommensurate phase of $Sr_2Nb_2O_7$ with the same incidence as in Fig. 12 but from a different specimen area. The symmetry is the same as in Fig. 3 but the intensity distribution is different.

ture. Fig. 14(*b*) shows a CBED pattern of the incommensurate phase obtained with the same incidence as in Fig. 14(*a*). The excitation errors between geometrically equivalent *Umweganregung* paths about **a*** to a kinematically forbidden reflection are the same. The kinematically forbidden reflections indicated by arrows show no intensity. This is a result of dynamical extinction for the four-dimensional crystal. The dynamical extinction does not appear as a line in Fig. 14(*b*) because the size of the diffraction disk is set small to avoid overlapping of the diffraction disks and the width of the dynamical extinction line exceeds the disk size. This experiment has revealed that dynamical extinction occurs from the four-dimensional glide plane for a displacively modulated crystal. Therefore, the dynamical extinction enables the space-group determination of the four-dimensional crystals or one-dimensional incommensurately modulated crystals.

4. Symmetry determination of five and six-dimensional crystals – quasicrystals

4.1. *Icosahedral quasicrystals – six-dimensional crystals*

Penrose (1974) demonstrated that the two-dimensional plane can be tiled with thin and fat rhombi to give a pattern with local fivefold rotation symmetries but with no translational symmetry. Mackay (1982) extended the tiling to three dimensions using acute and obtuse rhombohedra, which also resulted in the acquisition of local fivefold symmetries and in the vanishing of the translational symmetry. [The three-dimensional space-filling method was later completed by Ogawa (1985).] These, however, remained a matter of design or geometrical amusement until Schechtman *et al.* (1984) discovered an icosahedral symmetry presumably with long-range structural order in an alloy of Al_6Mn (nominal composition) using electron diffraction. Since then, the new class of structural order, which has no translational symmetry but has long-range structural order, has been called the 'quasicrystal'. Levine & Steinhardt (1984) showed that the quasilattice produces sharp diffraction patterns and succeeded in reproducing almost exactly the diffraction pattern obtained by Shechtman *et al.* (1984) using the Fourier transform of a quasiperiodic icosahedral lattice. In the course of analyzing X-ray and electron diffraction data, diffraction peaks could be successfully indexed by six independent vectors pointing to the vertices of an icosahedron. Then, it was found that the icosahedral quasicrystal can be described in terms of a regular crystal in six dimensions (*e.g.* Jarić, 1988). The quasicrystal is produced by the intersection of the six-dimensional crystal with an embedded three-dimensional hyperplane (the cut and projection technique).

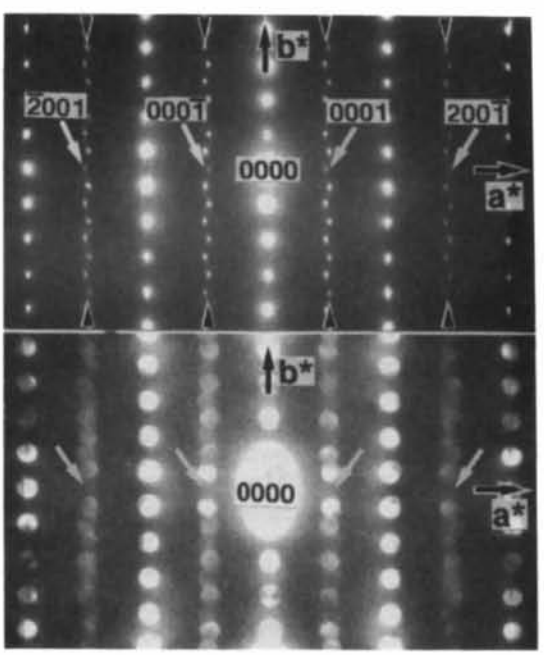

Fig. 14. (*a*) Usual electron diffraction pattern and (*b*) CBED pattern of the incommensurate phase of $Sr_2Nb_2O_7$ taken with [001] incidence at 60 kV. The kinemetically forbidden reflections indicated by short arrows show finite intensities in (*a*) but not in (*b*). No intensity in (*b*) is a result of dynamical extinction.

First, we investigated an alloy of the same composition (Tanaka, Terauchi, Hiraga & Hirabayashi, 1985) as that studied by Shechtman *et al.* (1984), their quasicrystalline grains later being found to be Al_4Mn. The grains of the quasicrystal were found to be less than 10 nm in size. All the CBED patterns obtained from a volume about 10 nm (diameter) × 100 nm (height) did not exhibit any fivefold or tenfold symmetry, although ordinary electron diffraction patterns showed tenfold symmetry. Small-area parallel-beam electron diffraction patterns taken from about 100 nm-diameter areas at an incidence along the tenfold axis revealed that the quasicrystal was highly strained. Three principal diffraction spots showed a zig-zag deviation from the radial line. Lubensky, Socolar, Steinhardt, Bancel & Heiney (1986) interpreted the result in terms of anisotropically quenched phason strains.

The addition of several percent of silicon to Al–Mn alloys caused a great increase in the degree of order of the quasicrystal. Bendersky & Kaufman (1986) prepared such a less-strained quasicrystalline $Al_{71}Mn_{23}Si_6$ alloy and determined its point group. They obtained fairly good zone-axis CBED patterns that showed symmetries of 10*mm*, 6*mm* and 2*mm* in ZOLZ disks and 5*m*, 3*m* and 2*mm* in HOLZ rings.

From these results, they identified the point group to be centrosymmetric $m\bar{3}\bar{5}$. Tanaka, Terauchi, Hiraga & Hirabayashi (1987) examined the crystallographic properties of a less-strained quasicrystalline $Al_{74}Mn_{20}Si_6$ alloy. Figs. 15(*a*) and (*b*) show 0.1 μm quasicrystalline grains of $Al_{74}Mn_{20}Si_6$. Electron diffraction patterns taken from a 110 nm-diameter area with a small incident-beam divergence of 0.03 mrad exhibited the innermost reflections with a lattice spacing of 2.27 nm. Among strong reflections, many weak diffraction spots appear, which were not observed in Al_4Mn and $Al_{71}Mn_{23}Si_6$ alloys. The reflections at high scattering angles have a stronger intensity than in Al_4Mn. These results indicate that the alloy $Al_{74}Mn_{20}Si_6$ has a much greater ordering than the other two. Figs. 16(*a*)–(*f*) show three pairs of CBED patterns taken from an area about 100 nm thick and about 3 nm diameter of an $Al_{74}Mn_{20}Si_6$ quasicrystal at an accelerating voltage of 60 kV. Each pair consists of a ZOLZ pattern and a HOLZ pattern. The former is produced almost by the interaction of ZOLZ reflections. Distinct symmetries are seen in several disks. Many HOLZ rings and Kikuchi bands are clearly seen in the HOLZ patterns. The profiles of Kikuchi bands are symmetric with respect to their centers [Figs. 16(*b*), (*d*) and (*f*)]. These results contrast strongly with those for Al_4Mn and indicate that the constituent atoms form a highly ordered arrangement of the quasicrystal.

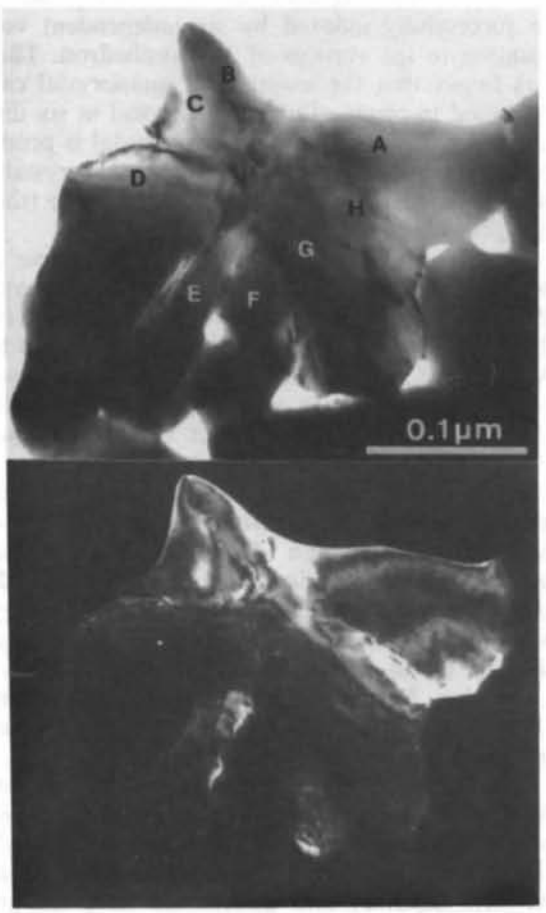

Fig. 15. (*a*) Bright-field and (*b*) dark-field electron micrographs of $Al_{74}Mn_{20}Si_6$ showing about 0.1 μm-diameter quasicrystalline grains.

The whole pattern of Fig. 16(*a*), formed by ZOLZ reflections, exhibits a tenfold rotation and two types of mirror symmetry, the resultant symmetry being expressed as 10*mm*. The whole pattern of Fig. 16(*b*), formed by HOLZ reflections, shows a fivefold symmetry and a type of mirror plane, the resultant symmetry being expressed as 5*m*. Figs. 16(*c*) and (*d*) show symmetries 6*mm* and 3*m*, respectively. Figs. 16(*e*) and (*f*) show symmetry 2*mm*.

It is known that there exist two icosahedral point groups 235 and $m\bar{3}\bar{5}$. The former is noncentrosymmetric and has no mirror symmetry but the latter is centrosymmetric. Table 10 shows diffraction groups expected from these point groups at the incident beam parallel to the fivefold or tenfold axis and their symmetries appearing in whole, BF, DF and $\pm G$ patterns. Projection diffraction groups and their symmetries, in which only the interaction between ZOLZ reflections is taken into account, are given in the second row. Diffraction groups obtained at other incident-beam orientations are omitted since these have been given in the references of Buxton *et al.* (1976) and Tanaka, Saito & Sekii (1983). The whole-pattern symmetries observed in the present quasicrystal agree with those expected from point group $m\bar{3}\bar{5}$, which was obtained by Bendersky & Kaufman (1986). Fig. 17(*a*) shows a zone-axis CBED pattern taken at an electron incidence along the threefold axis. Figs. 17(*b*) and (*c*) show a pair of $\pm G$ dark-field CBED patterns. The pattern of the $+G$ dark-field disk coincides with that of the $-G$ disk when the former is superposed on the latter with translation of $-2G$. This symmetry, 2_R, directly proves that the quasicrystal is centrosymmetric, again indicating the point group to be $m\bar{3}\bar{5}$. The lattice type was found to be primitive and no dynamical extinction was observed. Then, the space group of the alloy was determined as $Pm\bar{3}\bar{5}$.

Quasicrystals of Al–Mn alloys were produced by the melt-quenching method and were thermodynamically metastable. Tsai, Inoue & Masumoto (1987) first reported the existence of a stable icosahedral phase of $Al_{65}Cu_{20}Fe_{15}$. This alloy was found to have larger grains and to provide much better quality diffraction patterns with less phason strains than $Al_{74}Mn_{20}Si_6$. It was soon recognized that the lattice type of this phase and of some other Al–Cu–transition metal (TM) alloys is different from that of previously discovered ones. That is, the diffraction

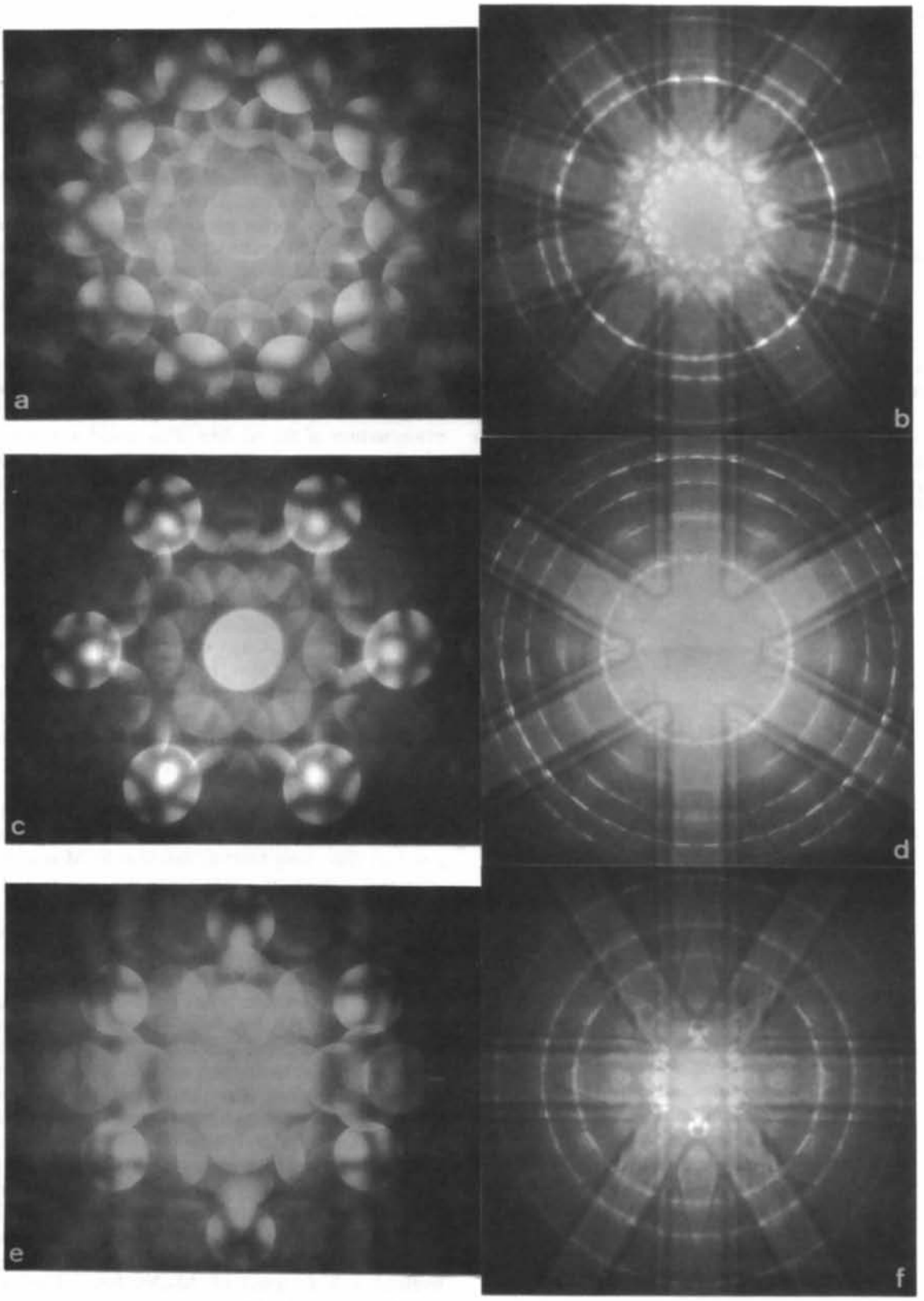

Fig. 16. Three pairs of ZOLZ and HOLZ whole patterns, showing symmetries (*a*) 10*mm*, (*b*) 5*m*, (*c*) 6*mm*, (*d*) 3*m*, (*e*) 2*mm* and (*f*) 2*mm*.

Table 10. *Diffraction groups of the icosahedral point groups and their CBED symmetries*

Point group	Diffraction group	BF pattern	Whole pattern	DF pattern	DF pattern
235	$5m_R$	$5m$	5	1 m_2	1 m_R 1
	(Projection) $5m1_R$	$10mm$	$5m$	$2=1_R$ $2m,m_2$	1 $m,1_R$ 1
$m\bar{3}\bar{5}$	10_Rmm_R	$10mm$	$5m$	1 m_2 m_v	2_R 2_Rm_2 2_Rm_v
	(Projection) $10mm1_R$	$10mm$	$10mm$	2 $2m,m_2$	21_R 21_Rm_v

pattern of Al–Cu–TM alloys displayed many additional spots to the twofold diffraction pattern of the melt-quenched alloys. It was found that the pattern was indexed either by all (six) even or all (six) odd or by a face-centered (F) lattice and that of Al–Mn alloys by a primitive lattice (Ebalard & Spaepen, 1989). All the icosahedral quasicrystals known to date belong to the point group $m\bar{3}\bar{5}$ but those with the noncentrosymmetric point group 235 have not been discovered.

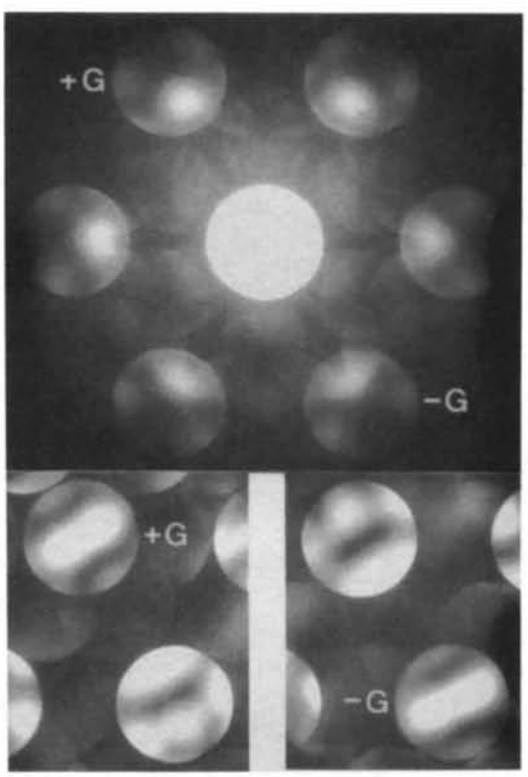

Fig. 17. (*a*) Zone-axis CBED pattern taken at an incidence along the threefold axis. (*b*) and (*c*) $\pm G$ dark-field CBED patterns.

4.2. *Decagonal quasicrystals – five-dimensional crystals*

The decagonal quasicrystal was first found by Bendersky (1985) in an alloy of Al–Mn using the electron diffraction technique. The phase has translational symmetry parallel to the tenfold axis and quasiperiodic long-range structural order perpendicular to the axis. The diffraction peaks were indexed by one vector parallel to the tenfold axis and four independent vectors pointing to the vertices of a decagon. Then, the decagonal quasicrystal is described in terms of a regular crystal in five dimensions.

Two space groups, $P10_5/m$ and $P10_5/mmc$, have been proposed by Bendersky (1986) and Yamamoto & Ishihara (1988), respectively, for the alloy. Owing to the low quality of the specimen, our CBED examination of the Al–Mn alloy could not determine whether the point group was $10/m$ or $10/mmm$. Furthermore, dynamical extinction owing to the screw axis was not observed in the CBED patterns. The quasicrystal and those of Al–M (M = Fe, Ru, Pt, Pd,...) alloys found at an early stage were thermodynamically metastable. Subsequently, thermodynamically stable decagonal phases were discovered in ternary alloys of $Al_{65}Cu_{15}Co_{20}$ (Tsai, Inoue & Masumoto, 1989*a*), $Al_{65}Cu_{20}Co_{15}$ (He, Wu & Kuo, 1989) and $Al_{70}Ni_{15}Co_{15}$ (Tsai, Inoue & Masumoto, 1989*b*). Electron microscopy of the decagonal phases revealed that the quasicrystalline grains were less than 10 nm in diameter and contained many planar defects. In electron diffraction patterns taken at electron incidences along the decagonal axis, only intense reflections were observed; weak reflections, which were observed for the icosahedral phases of good quality, were faint or not visible. Moreover, the observed reflection spots were not sharp and had irregular shapes. Space-group determination by CBED was barely successful only for Al–Ni–Co alloys – centrosymmetric $P10/mmm$.

Recently, Tsai, Inoue & Masumoto (1989*c*) produced a metastable but good-quality decagonal quasicrystal of $Al_{70}Ni_{15}Fe_{15}$. This alloy was found to be the first decagonal quasicrystal that could tolerate the symmetry examination using CBED. It is worthwhile pointing out that the metastable quasicrystal has a higher quality or a higher degree of order about quasicrystallinity than the stable quasicrystals. The space-group determination of the quasicrystalline $Al_{70}Ni_{15}Fe_{15}$ alloy by CBED was conducted by Saito, Tanaka, Tsai, Inoue & Masumoto (1992).

Fig. 18 shows a CBED pattern taken from an area of 3 nm diameter with a incidence parallel to the fivefold axis (c axis) of $Al_{70}Ni_{15}Fe_{15}$. The pattern clearly exhibits fivefold rotation and mirror symmetry, the total symmetry being expressed as $5m$. A

slowly varying intensity distribution in the disks indicates that the pattern is not affected by the interaction with HOLZ reflections but is formed by interactions between ZOLZ reflections. Thus, the projection approximation should be applied to the analysis of the pattern. Changes of the illuminated specimen area sometimes produced the patterns that were related to Fig. 18 by an inversion, indicating the existence of inversion domains. Fig. 19 shows possible pentagonal and decagonal point groups, which were constructed by consulting the trigonal and hexagonal point groups given in *International Tables for X-ray Crystallography* (1952). It can be seen that the point groups that satisfy the observed symmetry $5m$ in the projection approximation are 52, $5m$ and $\bar{1}0m2$. The point group 52 is a possibility because the horizontal twofold axis is equivalent to the vertical mirror plane in the projection approximation. Figs. 20(*a*) and (*b*) were taken from 3 nm-diameter areas with incidences *A* and *B*, respectively; these incidences are denoted in Fig. 18. Mirror symmetry perpendicular to the *c* axis is seen in Figs. 20(*a*) and (*b*). Since this symmetry requires a twofold axis or mirror plane perpendicular to the *c* axis to exist, point groups 52 and $\bar{1}0m2$ remain as possibilities. Fig. 20(*b*) exhibits symmetry $2mm$. Mirror symmetry parallel to the *c* axis requires the existence of a mirror plane parallel to the axis. Since the mirror plane does not exist in point group 52 but does exist in $\bar{1}0m2$, the point group of the alloy is determined to be $\bar{1}0m2$.

Examination of the usual diffraction patterns of the alloy revealed that the periodicity in the *c* direction is 0.4 nm and the lattice type is primitive; no dynamical extinction was observed. Then, the space group of $Al_{70}Ni_{15}Fe_{15}$ was determined to be $P\bar{1}0m2$. This is the first quasicrystal with a noncentrosymmetric space group.

Quasicrystals of $Al_{70}Ni_{10+x}Fe_{20-x}$ $(0 \le x \le 10)$ were investigated by CBED and transmission electron microscopy (Tanaka *et al.*, 1993). It was found that the alloys with $0 \le x \le 7$ belong to the noncentrosymmetric space group $P\bar{1}0m2$ and those with $7 < x \le 10$ to the centrosymmetric $P\bar{1}0/mmm$. High-resolution electron-microscope images detected the

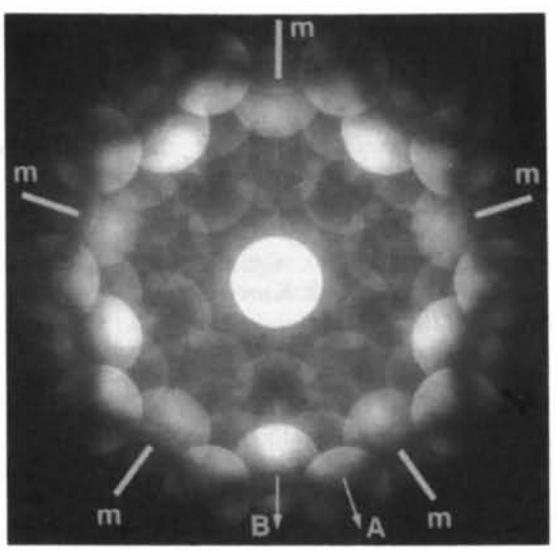

Fig. 18. CBED pattern of a melt-quenched $Al_{70}Ni_{15}Fe_{15}$ alloy taken from a 3 nm area at an incidence parallel to the decagonal axis. Note that the pattern shows fivefold rotation and mirror symmetry, total symmetry being denoted as $5m$.

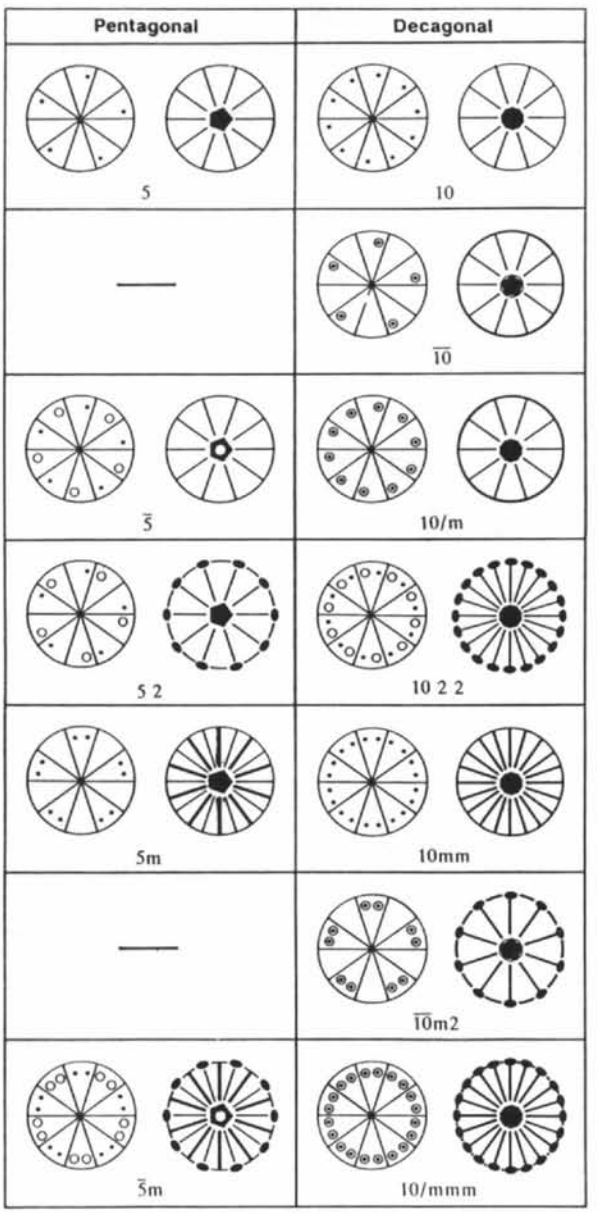

Fig. 19. Pentagonal and decagonal point groups constructed by analogy with trigonal and hexagonal point groups.

specific pentagonal atom cluster in all the alloys investigated. The change in space group takes place at $x \simeq 7.5$ upon the sudden decrease of the domain size or the rapid mixing of the atom clusters with positive and negative polarities. Dark-field microscopy of $Al_{70}Ni_{15}Fe_{15}$ alloys (Tsuda *et al.*, 1992) revealed that there exist inversion domains and the domain boundaries accompany an antiphase shift of $c/2$.

It must be specially mentioned that all the early discoveries on quasicrystals were performed by electron microscopy with electron diffraction. A variety of space groups in quasicrystals is expected to be discovered in future studies.

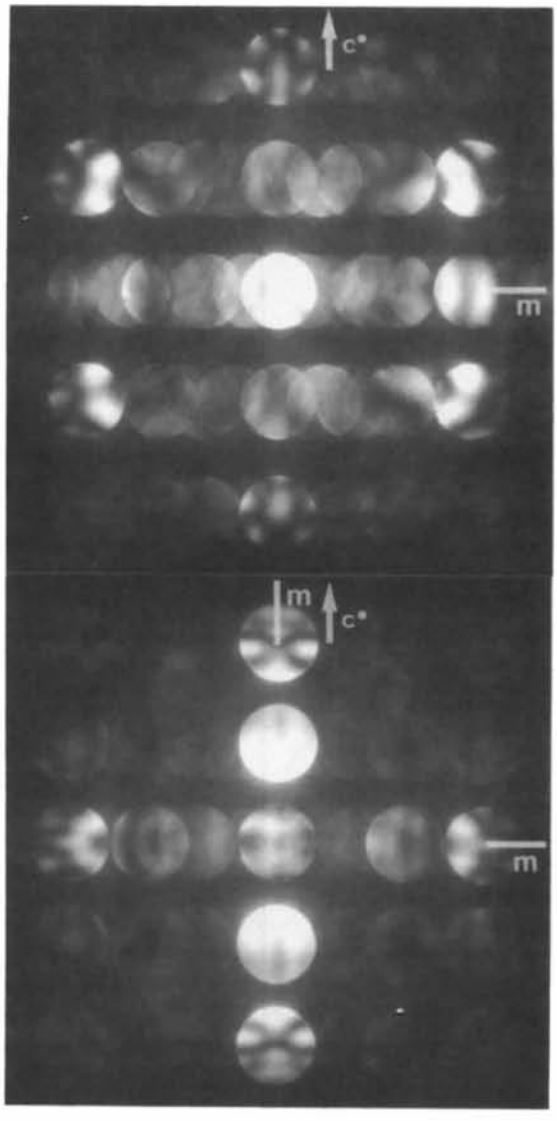

Fig. 20. CBED pattern of a melt-quenced $Al_{70}Ni_{15}Fe_{15}$ alloy taken from a 3 nm area at incidences (*a*) *A* and (*b*) *B*, which are perpendicular to the decagonal axis (*c* axis) and indicated in Fig. 18. (*a*) Mirror symmetry perpendicular to the *c* axis is seen, forming symmetry *m*. (*b*) Mirror symmetry both perpendicular and parallel to the *c* axis is seen, forming symmetry *2mm*.

5. Crystal-structure determination

The CBED method has the following advantages compared to the X-ray and neutron diffraction methods for crystal structure analysis. Firstly, the CBED method can be used to obtain diffraction patterns from a small specimen area that is a few nm in diameter. Then, it is possible to determine not only structures of perfect crystals but also local structures that change with position. Secondly, the CBED intensities possess information about the phases of structure factors because of strong dynamical diffraction effects. This fact contrasts strongly with X-ray and neutron cases, in which the kinematical diffraction theory is applicable and information about the phases is lost. Thirdly, the raw intensity data of the CBED pattern are of good enough quality to be compared directly to theoretical intensities and do not need many corrections, which have to be carefully made in the case of X-ray single-crystal structure analysis.

Vincent *et al.* (1984) first applied the CBED method to the determination of the atom positions of AuGeAs. They estimated the experimental intensities of the HOLZ reflections recorded on negative films using their eyes. They determined the positional parameters by fitting the theoretical intensities calculated under a quasikinematical approximation with the experimental ones. Vincent & Exelby (1990) applied the same method to the structure determination of a metastable Al–Ge phase. Tanaka & Tsuda (1990, 1991) refined the structural parameters (the rotation angle of the octahedron and the Debye–Waller factor) of the low-temperature phase of $SrTiO_3$, which is known to undergo a typical second-order phase transformation, on the basis of the dynamical theory of electron diffraction. Other attempts to refine positional or occupational parameters have been made by Taftø & Metzger (1985), Vincent & Bird (1986), Gjønnes, Boe & Gjønnes (1990) and Tomokiyo & Kuroiwa (1990).

Recently, the automatic matching of experimental and theoretical CBED patterns has been challenged by the minimization of an *R* factor by a steepest-descent method (Marthinsen, Høier & Bakken, 1991), the simplex method (Zuo & Spence, 1991), the quasi-Newton method (Bird & Saunders, 1991) and the Marquardt method (Tanaka & Tsuda, 1991). Bird & Saunders (1992*a*,*b*) studied the sensitivity and accuracy of CBED pattern matching and tested an *ab initio* determination method of the structure factors on the [110] axis of GaP using simulated patterns as ideal experimental data. The refinement of

low-order crystal structure factors is described in the literature by Spence (1993).

For quantitative study or structure determination by CBED, the most important points are:

(i) *High speed dynamical calculations.* A calculation to obtain the intensity for a point of a CBED pattern needs to use more than 100 beams. For the fitting of the calculated CBED pattern with an experimental one, two-dimensional calculations at different incident-beam orientations in the k_x and k_y directions are needed with repetition of these until a good match is obtained. Such calculations have recently been carried out conveniently by a laboratory-use workstation at the cost of little more time than a supercomputer would need. To reduce computing time, however, the use of a low accelerating voltage of incident electrons and the application of the perturbation method and the Bethe potential method to the calculation are still important.

(ii) *Accurate intensity recording.* CBED patterns usually have a wide dynamic range in intensity. It is difficult to record the CBED intensities correctly with standard negative films owing to their nonlinear properties and narrow dynamic range. The use of a slow-scan charge-coupled device (Mochel & Mochel, 1986; Mooney, Fan, Meyer, Truong & Krivanek, 1990) or an imaging plate (Ichihara *et al.*, 1984; Mori, Oikawa, Harada & Miyahara, 1990; Oikawa, Mori, Takano & Ohnishi, 1990) is necessary for the accurate recording of the intensity.

(iii) *Subtraction of inelastically scattered intensities.* To obtain accurate experimental data to be compared with calculated intensities, inelastically scattered intensities should be subtracted. Tanaka & Tsuda (1991) demonstrated for silicon and FeS_2 using a sector-type energy filter how plasmon-loss intensities are harmful to the CBED patterns. It had been suggested that phonon scattering was worse than plasmon scattering because the former causes the interband transition, the latter the intraband transition; however, their experiment revealed that it is essential to remove plasmon scattering to decrease diffuse background and that phonon scattering appears to spoil the patterns very little. Recently, an electron microscope with an ω energy filter to cut off plasmon-loss electrons has been developed (Mayer, Spence & Möbus, 1991).

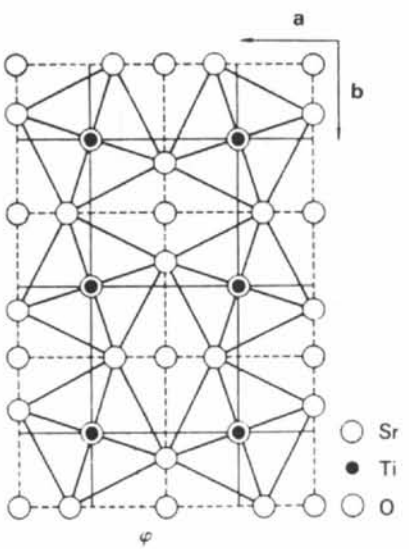

Fig. 21. Projection of the low-temperature form of $SrTiO_3$ along the c axis. The oxygen octahedron rotates an angle φ from that of the high-temperature form.

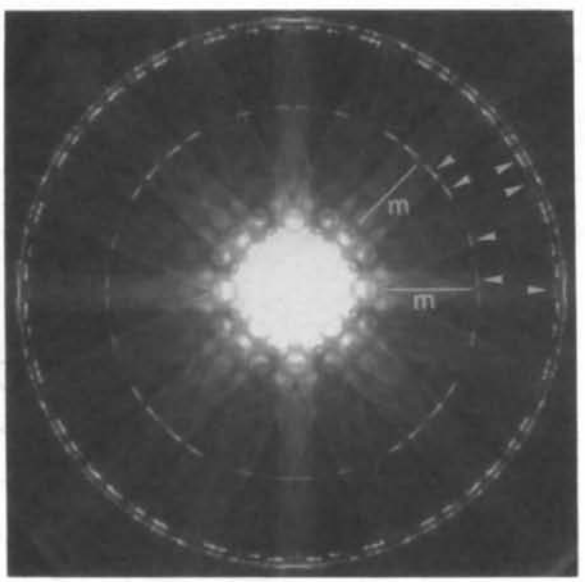

Fig. 22. [001] zone-axis CBED pattern taken at a temperature of 85 K and an accelerating voltage of 84 kV.

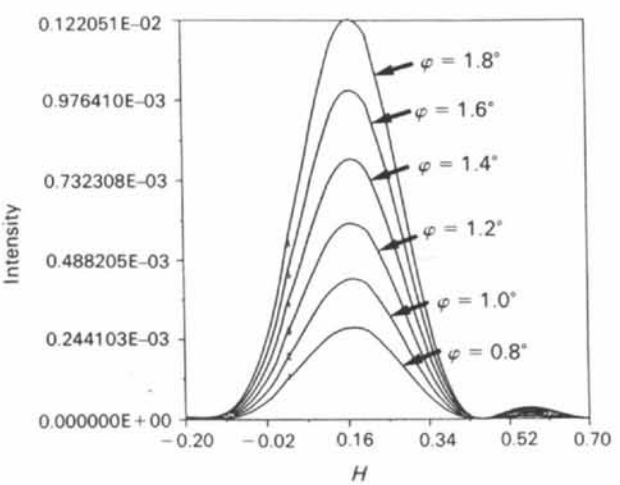

Fig. 23. Calculated intensity profiles of the 1,14,1 FOLZ reflection as a function of rotation angle.

It is shown here, for $SrTiO_3$, that structure refinement can successfully be conducted by the CBED method (Tanaka & Tsuda, 1990). $SrTiO_3$ undergoes a second-order phase transformation at 110 K from the high-temperature phase of *Pm3m* to the low-temperature phase of *I4/mcm*. The high-temperature phase has the cubic perovskite structure, in which an oxygen octahedron surrounds a Ti atom. In the low-temperature phase, the oxygen octahedron rotates slightly owing to the condensation of the R_{25} phonon mode (Fig. 21) of the high-temperature phsae. The positions of Sr and Ti atoms are considered unchanged. Therefore, structure analysis of the low-temperature phase implies determination of the rotation angle φ of the octahedron and the Debye–Waller factor B of the O atoms, where B is assumed to be isotropic.

Fig. 22 shows a [001] zone-axis CBED pattern taken at 85 K and at an accelerating voltage of 84 kV, exhibiting *4mm* symmetry. The first-order Laue-zone (FOLZ) reflections appear only at the low-temperature phase or originate from the rotation of the oxygen octahedra. The reflections used were four FOLZ reflections (1,14,1, 3,14,1, 7,12,1 and 9,10,1) and three second-order Laue-zone (SOLZ) reflections (5,19,2, 7,19,2 and 14,14,2), which are indicated by arrows. In the case of SOLZ reflections, only the outer peaks were used because these peaks were found to originate from the rotation of the oxygen octahedra from the analysis of the Bloch states formed by ZOLZ reflections. Fig. 23 shows the calculated intensity profiles of the 1,14,1 FOLZ reflection as a function of the rotation angle φ, the calculation being carried out using 126 beams. It is seen that the intensity increases monotonically with the increase in φ without changing the peak position. It was found that the intensities of the outer peaks of the SOLZ reflections decrease with increasing φ. The accelerating voltage was determined in advance using a standard silicon specimen. The specimen thickness was determined by fitting the simulation patterns with the ZOLZ reflection pattern in Fig. 22. The HOLZ reflection intensities were calculated as functions of the rotation angle φ and the Debye–Waller factor B. Fig. 24 shows the reliability factor $R = \sum_g |I_g(\text{obs.}) - I_g(\text{cal.})| / I_g(\text{obs.})$, where the abscissa is

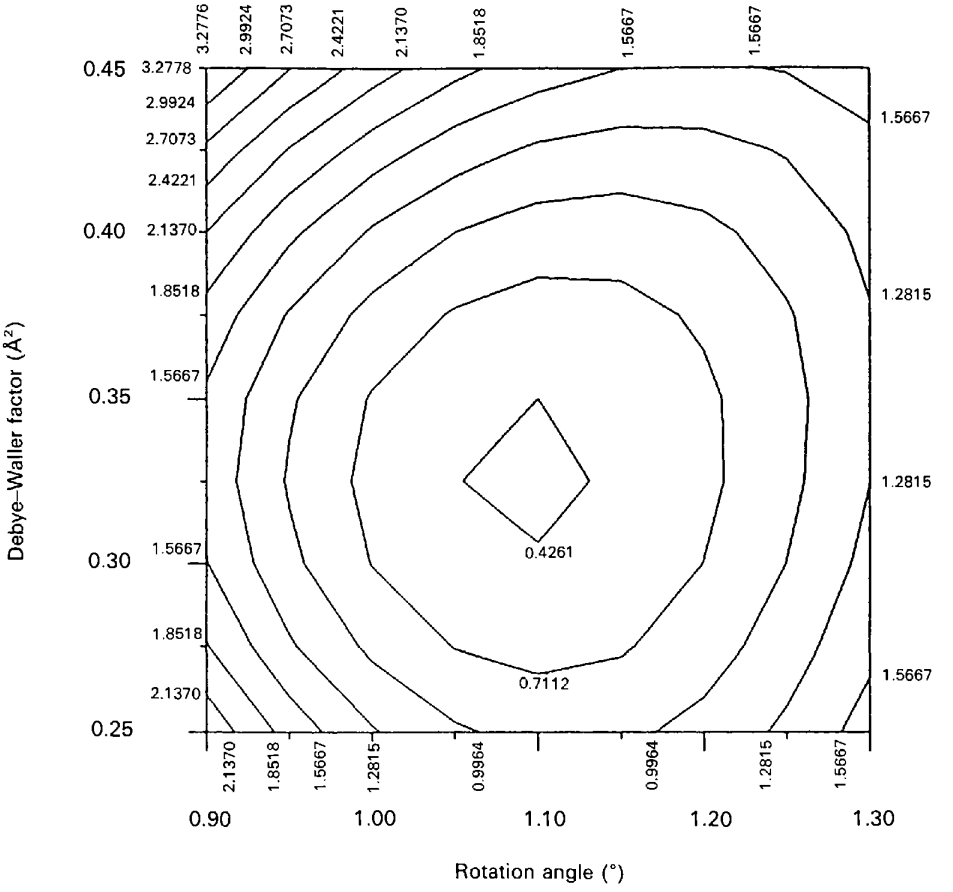

Fig. 24. Contour map of the reliability factor R, the abscissa and ordinate being the rotation angle and the Debye–Waller factor, respectively.

the rotation angle and the ordinate the Debye–Waller factor. The two parameters were determined to be $\varphi = 1.1\ (2)^\circ$ and $B = 0.325\ (100)\ \text{Å}^2$ by fitting the experimental profiles with theoretical ones (Tsuda & Tanaka, 1994). Unoki & Sakudo (1967) and Müller, Beringer & Waldner (1968) determined the rotation angle at 78 K as 1.4 (1) and 1.25°, respectively, from electron-spin resonance experiments. Shirane & Yamada (1969) determined the angle to be 1.37 (35)° at 78 K from neutron diffraction. It is evident that the present result is consistent with these results when the temperature difference is considered.

The result is sufficient to show that crystal structure analysis by convergent-beam electron diffraction is feasible. This method is expected to lead to the development of a new field of nanometer-scale crystal structure refinement. Its application will extend to both perfect and imperfect crystals.

Concluding remarks

The convergent-beam electron diffraction method has been shown to be a very powerful technique to determine the symmetries of usual three-dimensional crystals and of higher-dimensional crystals. The method is developing further as a technique for determining crystal structures of nanometer-scale areas.

References

BENDERSKY, L. A. (1985). *Phys. Rev. Lett.* **55**, 1461–1467.

BENDERSKY, L. A. (1986). *J. Phys.* (*Paris*), **47**, pp. c3–457.

BENDERSKY, L. A. & KAUFMAN, M. J. (1986). *Philos. Mag.* B**53**, L75–L80.

BIRD, D. M. & SAUNDERS, M. (1991). *Microbeam Analysis* 1991, edited by D. G. HOWITT, pp. 153–156. San Francisco Press.

BIRD, D. M. & SAUNDERS, M. (1992*a*). *Ultramicroscopy*, **45**, 241–251.

BIRD, D. M. & SAUNDERS, M. (1992*b*). *Acta Cryst.* A**48**, 555–562.

BUXTON, B. F., EADES, J. A., STEEDS, J. W. & RACKHAM, G. M. (1976). *Philos. Trans. R. Soc. London*, **281**, 171–194.

COWLEY, J. M. & MOODIE, A. F. (1959). *Acta Cryst.* **12**, 360–367.

COWLEY, J. M., MOODIE, A. F., MIYAKE, S., TAKAGI, S. & FUJIMOTO, F. (1961). *Acta Cryst.* **14**, 87–88.

EADES, J. A. (1988*a*). *EUREM*88, *Inst. Phys. Conf. Ser.* **93**, 3–12.

EADES, J. A. (1988*b*). *Microbeam Analysis* 1988, edited by D. E. NEWBURY, pp. 75–80. San Francisco Press.

EADES, J. A. (1992). *Electron Diffraction Techniques*, Vol. 1, edited by J. M. COWLEY, ch 7. IUCr/Oxford Univ. Press.

EBALARD, S. & SPAEPEN, F. (1989). *J. Mater, Res.* **4**, 39–43.

GJØNNES, J., BOE, N. & GJØNNES, K. (1990). *Proc. XIIth International Congress on Electron Microscopy, Seattle, USA*, edited by L. D. PEACHY & D. B. WILLIAMS, Vol. 2, pp. 516–517. San Francisco Press.

GJØNNES, J. & MOODIE, A. F. (1965). *Acta Cryst.* **19**, 65–67.

GOODMAN, P. (1975). *Acta Cryst.* A**31**, 804–810.

GOODMAN, P. (1984). *Acta Cryst.* A**40**, 635–642.

GOODMAN, P. & JOHNSON, A. W. S. (1977). *Acta Cryst.* A**33**, 126–133.

GOODMAN, P. & LEHMPFUHL, G. (1964). *Z. Naturforsch. Teil A*, **19**, 818–820.

GOODMAN, P. & LEHMPFUHL, G. (1965). *Z. Naturforsch. Teil A*, **20**, 110–114.

GOODMAN, P. & SECOMB, T. W. (1977). *Acta Cryst.* A**33**, 997–1001.

HE, L. X., WU, Y. K. & KUO, K. H. (1989). *J. Mater. Sci. Lett.* **7**, 1284–1286.

ICHIHARA, S., HAYAKAWA, S., SAGA, S., HOSHINO, M., SAKUMA, S., IKEDA, M., YAMAGUCHI, H., HANAICHI, T. & KAMIYA, Y. (1984). *J. Electron Microsc.* **33**, 255–257.

International Tables for X-ray Crystallography (1952). Vol. I. Birmingham: Kynoch Press.

JANNER, A. & JANSSEN, T. (1980). *Acta Cryst.* A**36**, 399–408, 408–415.

JARIĆ, M. V. (1988). Editor. *Introduction to Quasicrystals*, Vol. 1. New York: Academic Press.

KOSSEL, W. & MÖLLENSTEDT, G. (1939). *Ann. Phys.* (*Leipzig*), **36**, 113–140.

LEVINE, D. & STEINHARDT, P. J. (1984). *Phys. Rev. Lett.* **53**, 2477–2480.

LUBENSKY, T. C., SOCOLAR, J. E. S., STEINHARDT, P. J., BANCEL, P. A. & HEINEY, P. A. (1986). *Phys. Rev. Lett.* **57**, 1440–1443.

MACKAY, A. L. (1982). *Physica* (*Utrecht*), **114A**, 609–613.

MARTHINSEN, K., HØIER, R. & BAKKEN, L. N. (1990). *Proc. XIIIth International Congress on Electron Microscopy, Seattle, USA*, edited by L. D. PEACHY & D. B. WILLIAMS, Vol. 2, pp. 492–493. San Francisco Press.

MAYER, J., SPENCE, J. C. H. & MÖBUS, G. (1991). *Proc. 49th Annual Meeting of the Electron Microscopy Society of America*, edited by G. W. BAILEY, pp. 786–787. San Francisco Press.

MIYAKE, S., TAKAGI, S. & FUJIMOTO, F. (1960). *Acta Cryst.* **13**, 360–361.

MOCHEL, M. E. & MOCHEL, J. M. (1986). *Proc. 44th Annual Meeting of the Electron Microscopy Society of America*, pp. 616–617. San Francisco Press.

MOONEY, P. E., FAN, G. Y., MEYER, C. E., TRUONG, K. V. & KRIVANEK, O. L. (1990). *Proc. XIIth International Congress on Electron Microscopy, Seattle, USA*, edited by L. D. PEACHY & D. B. WILLIAMS, Vol. 1, pp. 164–165. San Francisco Press.

MORI, N., OIKAWA, T., HARADA, Y. & MIYAHARA, J. (1990). *J. Electron Microsc.* **39**, 195–207.

MÜLLER, K. A., BERINGER, W. & WALDNER, F. (1968). *Phys. Rev. Lett.* **21**, 814–817.

OGAWA, T. (1985). *J. Phys. Soc. Jpn*, **54**, 3205–3208.

OIKAWA, T., MORI, N., TAKANO, N. & OHNISHI, M. (1990). *J. Electron Microsc.* **39**, 433–436.

PENROSE, R. (1974). *Bull. Inst. Math. Appl.* **10**, 266–271.

POGANY, A. P. & TURNER, P. S. (1968). *Acta Cryst.* A**24**, 103–109.

SAITO, M., TANAKA, M., TSAI, A. P., INOUE, A. & MASUMOTO, T. (1992). *Jpn. J. Appl. Phys.* **31**, L109–L112.

SHECHTMAN, I., BLECH, I., GRATIAS, D. & CAHN, J. W. (1984). *Phys. Rev. Lett.* **53**, 1951–1953.

SHIRANE, G. & YAMADA, Y. (1969). *Phys. Rev.* **177**, 858–863.

SPENCE, J. C. H. (1993). *Acta Cryst.* A**49**, 231–260.

SPENCE, J. C. H. & ZUO, J. M. (1992). *Electron Microdiffraction*. New York: Plenum.

STEEDS, J. W., BIRD, D. M., EAGLESHAM, D. J., MCKERNEN, S., VINCENT, R. & WITHERS, R. L. (1985). *Ultramicroscopy*, **17**, 97–110.

STEEDS, J. W., RACKHAM, G. M. & SHANNON, M. D. (1978). *Inst. Phys. Conf. Ser.* **41**, 135–139.

STEEDS, J. W. & VINCENT, R. (1983). *J. Appl. Cryst.* **16**, 317–324.

TAFTØ, T. & METZGER, T. H. (1985). *J. Appl. Cryst.* **18**, 110–116.

TANAKA, M. (1989). *J. Electron Microsc. Tech.* **13**, 27–39.

TANAKA, M., SAITO, R. & SEKII, H. (1983). *Acta Cryst.* A**39**, 357–368.

TANAKA, M., SEKII, H. & NAGASAWA, T. (1983). *Acta Cryst.* A**39**, 825–837.
TANAKA, M., SEKII, H. & OHI, K. (1985). *Jpn. J. Appl. Phys.* **24**, Supplement 24-2, pp. 814–816.
TANAKA, M., TAKAYOSHI, H., ISHIDA, M. & ENDOH, Y. (1985). *J. Phys. Soc. Jpn*, **54**, 2970–2974.
TANAKA, M. & TERAUCHI, M. (1985). *Convergent-Beam Electron Diffraction*, p. 192. Tokyo: JEOL-Maruzen.
TANAKA, M. & TERAUCHI, M., HIRAGA, K. & HIRABAYASHI, M. (1985). *Ultramicroscopy*, **17**, 279–285.
TANAKA, M. & TERAUCHI, M., HIRAGA, K. & HIRABAYASHI, M. (1987). *Acta Cryst.* B**43**, 494–501.
TANAKA, M., TERAUCHI, M. & KANEYAMA, T. (1988). *Convergent-Beam Electron Diffraction* II, p. 284. Tokyo: JEOL-Maruzen.
TANAKA, M., TERAUCHI, M. & KANEYAMA, T. (1991). *J. Electron Microsc.* **40**, 211–220.
TANAKA, M., TERAUCHI, M. & SEKII, H. (1987). *Ultramicroscopy*, **21**, 245–250.
TANAKA, M. & TSUDA, K. (1990). *Proc. XIIth International Congress on Electron Microscopy, Seattle, USA*, edited by L. D. Peachy & D. B. Williams, Vol. 2, pp. 518–519. San Francisco Press.
TANAKA, M. & TSUDA, K. (1991). *Microbeam Analysis* 1991, edited by D. G. HOWITT, pp. 145–146. San Francisco Press.
TANAKA, M., TSUDA, K., TERAUCHI, M., FUJIWARA, A., TSAI, A. P., INOUE, A. & MASUMOTO, T. (1993). *J. Non-Cryst. Solids*, **153&154**, 98–102.
TERAUCHI, M., TAKAHASHI, M. & TANAKA, M. (1994). *Acta Cryst.* A. In the press.
TERAUCHI, M. & TANAKA, M. (1993). *Acta Cryst.* A**49**, 722–729.
TINNAPPEL, A. (1975). PhD thesis, Technische Univ. Berlin, Germany.
TOMOKIYO, Y. & KUROIWA, T. (1990). *Proc. XIIth International Congress on Electron Microscopy, Seattle, USA*, edited by L. D. PEACHY & D. B. WILLIAMS, Vol. 2, pp. 526–527. San Francisco Press.
TSAI, A. P., INOUE, A. & MASUMOTO, T. (1987). *Jpn. J. Appl. Phys. Lett.* **26**, L1505–L1507.
TSAI, A. P., INOUE, A. & MASUMOTO, T. (1989*a*). *Mater. Trans. Jpn Inst. Met.* **30**, 300–304.
TSAI, A. P., INOUE, A. & MASUMOTO, T. (1989*b*). *Jpn Inst. Met.* **30**, 463–473.
TSAI, A. P., INOUE, A. & MASUMOTO, T. (1989*c*). *Mater. Trans. Jpn Inst. Met.* **30**, 150–154.
TSUDA, K., SAITO, M., TANAKA, M., TSAI, A. P., INOUE, A. & MASUMOTO, T. (1992). *Jpn. J. Appl. Phys.* **32**, 129–134.
TSUDA, K. & TANAKA, M. (1994). *Acta Cryst.* A. Submitted.
UNOKI, H. & SAKUDO, T. (1967). *J. Phys. Soc. Jpn*, **23**, 546–522.
VINCENT, R. & BIRD, D. M. (1986). *Philos. Mag. A***53**, L35–L40.
VINCENT, R., BIRD, D. M. & STEEDS, J. W. (1984). *Philos. Mag.* A**50**, 745–763, 765–786.
VINCENT, R. & EXELBY, D. R. (1990). *Proc. XIIth International Congress on Electron Microscopy, Seattle, USA*, edited by L. D. PEACHY & D. B. WILLIAMS, Vol. 2, pp. 524–525. San Francisco Press.
WOLFF, P. M. DE (1974). *Acta Cryst.* A**30**, 777–785.
WOLFF, P. M. DE (1977). *Acta Cryst.* A**33**, 493–497.
WOLFF, P. M. DE, JANSSEN, T. & JANNER, A. (1981). *Acta Cryst.* A**37**, 625–636.
YAMAMOTO, A. (1982). *Acta Cryst.* A**38**, 87–92.
YAMAMOTO, A. & ISHIHARA, K. N. (1988). *Acta Cryst.* A**44**, 707–714.
YAMAMOTO, A., JANSSEN, T., JANNER, A. & DE WOLFF, P. M. (1985). *Acta Cryst.* A**41**, 528–530.
YAMAMOTO, N. (1982). *Acta Cryst.* A**38**, 780–789.
YAMAMOTO, N. (1988). *Solid State Phys.* **23**, 547–556.
YAMAMOTO, N. & ISHIZUKA, K. (1983). *Acta Cryst.* B**39**, 210–216.
ZUO, J. M. & SPENCE, J. C. H. (1991). *Ultramicroscopy*, **35**, 185–196.